Ann. Geophys., 44, 331–351, 2026
https://doi.org/10.5194/angeo-44-331-2026

Annales Geophysicae
Open Access

Studies of noctilucent clouds from the stratosphere during the 2024 TRANSAT balloon flight

Peter Dalin[1], **Hidehiko Suzuki**[2], **Nikolay Pertsev**[3], **Vladimir Perminov**[3], **Linda Megner**[4], **Johan Kero**[1], **Peter Voelger**[1], **Jonas Hedin**[4], **Gerd Baumgarten**[5], **Anne Réchou**[6], and **Denis Efremov**[7]

[1]Swedish Institute of Space Physics, Kiruna, Sweden
[2]School of Science and Technology, Meiji University, Kawasaki, Japan
[3]A.M. Obukhov Institute of Atmospheric Physics RAS, Moscow, Russia
[4]Department of Meteorology (MISU), Stockholm University, Stockholm, Sweden
[5]Leibniz Institute of Atmospheric Physics, Rostock University, Kühlungsborn, Germany
[6]Lacy Laboratory of Atmosphere and Cyclones, Université de La Réunion, Réunion, France
[7]Aerospace Laboratory "Stratonautica", Moscow, Russia

Correspondence: Peter Dalin (pdalin@irf.se)

Received: 19 November 2025 – Discussion started: 11 December 2025
Revised: 17 April 2026 – Accepted: 19 April 2026 – Published: 18 May 2026

Abstract. A transatlantic scientific balloon flight (TRANSAT) was conducted between 22 and 26 June 2024. The TRANSAT balloon, operated by the French Space Agency (CNES), floated in the stratosphere at approximately 40 km altitude between Esrange (Sweden) and Baffin Island (Canada) for about 3.8 d. The scientific payload comprised nine instruments, including an optical imager for noctilucent cloud (NLC) studies from the Swedish Institute of Space Physics. The NLC imager consisted of three identical visible-range optical cameras, one of which operated successfully throughout the entire flight, capturing thousands of NLC images. The TRANSAT balloon campaign was supported by ground-based lidar measurements and spaceborne observations from the Swedish MATS satellite. Here, we describe the technical characteristics of the balloon experiment and present early results. Nearly continuous observations of NLC were obtained during the entire flight. A localized warm region in the mesopause was identified as the cause of temporary NLC disappearance, while complex NLC structures exhibiting different motions were found to probably result from horizontal wind rotation with altitude within the mesopause region.

1 Introduction

Noctilucent clouds (NLC) are the highest clouds in the Earth's atmosphere, forming in the summer mesopause region between 80 and 90 km altitude at middle and polar latitudes in both hemispheres. They consist of water-ice particles with radii of 30–100 nm that scatter sunlight, making the clouds visible against the twilight sky. NLCs are typically observed from May to September in the Northern Hemisphere and from November to February in the Southern Hemisphere (Gadsden and Schröder, 1989; Liu et al., 2016). When observed from space, these clouds are traditionally called Polar Mesospheric Clouds (PMC) (Thomas, 1984).

NLC and PMC are systematically studied using ground-based optical cameras, spectrographs, lidars as well as dedicated spaceborne instruments (e.g., Karlsson and Gumbel, 2005; Dalin et al., 2008; Bailey et al., 2009; Fiedler et al., 2011; DeLand and Thomas, 2015; Tsuda et al., 2022; Wallis et al., 2025). In addition, irregular campaign-based NLC observations are carried out using sounding rockets and aircraft (Zadorozhny et al., 1993; Gumbel and Witt, 2001; Reimuller et al., 2011; Suzuki et al., 2022; Pertsev et al., 2024). Each observational technique has specific advantages and limitations. In particular, ground-based imagers offer high horizontal (~ 20 m) and temporal (~ 1 s) resolution (Dalin et al., 2010; Baumgarten and Fritts, 2014), and lidars provide high vertical resolution (50–150 m; Baumgarten et al., 2009), but both are restricted by tropospheric weather and limited geographic coverage. Conversely, satellite observations deliver global PMC coverage but suffer from low spatial (∼ 1 km) and temporal (minutes to hours) resolution. Moreover, sun-synchronous satellites introduce large spatial gaps (hundreds of km) between adjacent orbits at mid- and subpolar latitudes (45–60° N) due to a spacecraft orbiting the Earth. Consequently, no single existing technique can fully resolve the microphysical and dynamical processes governing NLC/PMC.

Balloon-borne observations from stratospheric altitudes (25–40 km) have a potential for comprehensive studies of NLC on a regular basis. Such observations provide several advantages: independence from tropospheric weather, uninterrupted 24 h coverage, and proximity to the NLC layer (80–85 km), yielding the highest achievable spatial resolution. From this vantage point, both large-scale (up to 2500 km, limited by Earth's curvature) and small-scale (down to meters) NLC features can be observed. Furthermore, balloon-borne observations at 30–40 km altitude occur above the ozone-rich layer (20–25 km), thereby avoiding light absorption in the Chappuis band (400–650 nm).

To date, four balloon-borne experiments have been dedicated to NLC observations from the stratosphere (Miller et al., 2015; Dalin et al., 2019, 2020, 2022; Fritts et al., 2019). These missions have provided unique datasets for studying both large- and small-scale wave dynamics and turbulence within NLC layers. The motivation for the NLC experiment on board the 2024 TRANSAT flight are as follows:

1. Investigation of temporal-spatial variability of NLC at large- and small-scales in the subpolar and polar mesopause for several days.

2. Quantification of atmospheric gravity waves at large- and small-scales and turbulent processes, with modeling of propagation pathways and search for wave sources in the underlying atmosphere.

3. Gaining experience in conducting experiments in the stratosphere for several days.

In this study, we present results from a new long-duration balloon experiment aimed at investigating NLC in the polar mesopause. We describe the observation technique and instrumentation as well as early scientific findings. The stratospheric NLC observations were complemented by ground-based lidars and, for the first time, by spaceborne measurements from the Swedish MATS satellite. Additionally, temperature and water vapor data from the Aura/MLS satellite were used to characterize the mesopause environment during the TRANSAT flight, and JAWARA model data were employed to simulate the thermodynamic and wind conditions in support of the NLC observations.

2 Technique and method

2.1 Technical characteristics of the imager

The Stratospheric Observations of Noctilucent Clouds (SONC) experiment is a balloon-borne scientific mission designed to investigate NLC dynamics across a broad range of spatial scales – from large-scale structures (30–2500 km) to fine-scale features (5 m–30 km) – as well as the microphysical properties of NLC ice particles.

To achieve these objectives, three high-resolution, high-sensitivity Sony α7 Mark III cameras were used. Each camera has a full-frame 35 mm, 24-megapixel sensor (6000×4000 pixels). Two cameras were equipped with wide-angle lenses (field of view, FoV, $= 105.4° \times 81.8°$), while the third carried a narrow-angle lens (FoV $= 15.0° \times 10.1°$). This configuration, two wide-angle and one narrow-angle camera, provides a horizontal coverage of about 180° for studying mesospheric NLC structures up to 2500 km across, while simultaneously enabling spatial resolution as fine as about 5 m when viewing the NLC layer at 83 km from a 40 km altitude and 35° elevation angle. Note that such simultaneous access to both large and small scales is currently unattainable from either ground-based or satellite platforms. The three cameras formed the SONC imager, illustrated in Fig. 1. Each camera stored data on two 1 TB SD cards. Given the expected 4–5 d duration of the transatlantic flight and the storage limits, an image acquisition cadence of 50 s was chosen. This temporal resolution enables tracking the evolution of small-scale wave activity within the NLC layer as well as monitoring large-scale cloud dynamics. The optical axes of the two wide-angle cameras were inclined at 36° to the horizontal plane in order to minimize light contamination from bright tropospheric scattering and from above coming from a big white balloon envelope (∼ 70 m in diameter). The narrow-angle camera was tilted at 35° to the horizontal plane to resolve fine-scale structures of NLC.

Sony α7 Mark III camera has a standard Micro USB terminal for power supplying, battery charging and USB communications, into which an external trigger can be connected to activate the shutter button. For this purpose, we have developed an external trigger (gray box shown in Fig. 1) that simultaneously transmits the trigger signal to all three NLC cameras at a certain cadence time (50 s in this experiment). Thus, automatic shooting is carried out by the three cameras throughout the balloon flight. In addition, this external device distributes power to all three cameras from an external power supply (a chemical battery on the gondola).

Automatic exposure bracketing was applied, capturing 5 images sequentially with exposure times varying between $1/1600$ and 1.6 s. This approach accommodated a wide dynamic range of NLC brightness under variable atmospheric background illumination conditions. One wide-angle camera (left in Fig. 1) operated flawlessly throughout the 3.8 d flight, producing a total of about 40 000 images. The other

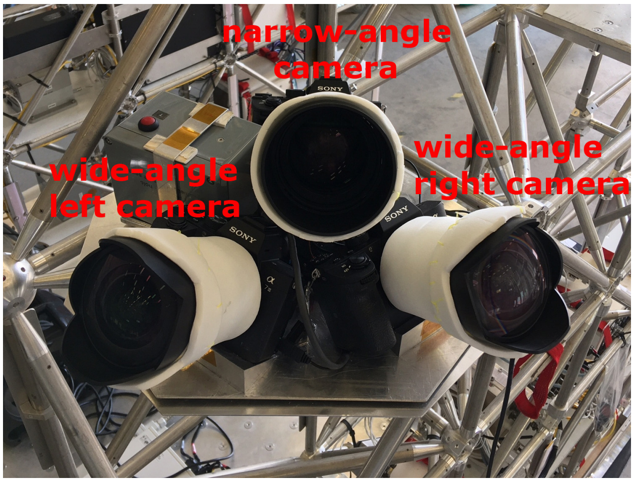

Figure 1. The SONC imager consists of three Sony α7 Mark III cameras and the electronic control unit (gray box with red button). Two cameras are equipped with wide-angle lenses, and one with a narrow-angle lens positioned between them. The instrument was used to observe noctilucent clouds during the TRANSAT transatlantic balloon flight (22–26 June 2024).

wide-angle and the narrow-angle cameras functioned for the first 13 and 12 h, respectively, before ceasing operation for unknown reasons. The imager survived the gondola landing on the ice of Baffin Island without damage. Post-flight tests of all the cameras and electronics confirmed full functionality of the SONC imager and no performance degradation. It should be noted that all three cameras had already been in the stratosphere for about 13 h at low temperatures of −30 °C and were functioning normally (Dalin et al., 2022). Taking into account the previous positive balloon-borne experiment, it was decided to use all three cameras for the long-duration TRANSAT flight in the stratosphere. Also note that SONY α7 Mark III cameras are commercial cameras that are not designed for a flight in the stratosphere in 24/7 sunlight, at low temperatures and low thermal conductivity due to rarefied air. The electronics inside the two cameras could freeze or overheat. This is the most likely reason for the failure of these two cameras after 12 h of the flight.

2.2 Technical characteristics of the TRANSAT balloon flight

The TRANSAT mission is a long-duration stratospheric balloon flight organized and operated by the French Space Agency (CNES) for multidisciplinary atmospheric and cosmic research. The gondola, named Carmen, had a total mass of about 900 kg and carried nine scientific instruments. Two of these were from Sweden: the SONC imager and an infrasound instrument dedicated to studies of infrasound atmospheric waves and their sources. The infrasound experiment and its scientific results will be described in a separate paper.

The Carmen gondola utilized a three-axis motorized gimbal stabilized platform, providing an elevation-angle stability of 0.15°, an absolute azimuth pointing accuracy of 1° and a stability of ±10 arcmin around it. Because stratospheric balloons rotate continuously, such stabilization was critical to avoid image smearing and to maintain consistent NLC monitoring at fine and large scales.

As the transatlantic flight took place under solstice conditions with continuous solar illumination, scientific instruments were mounted behind a solar shield to prevent overheating and stray-light interference. To ensure continuous shading, the gondola was slowly rotated to keep the solar shield facing the Sun throughout the flight. Due to different scientific experiments onboard requiring different pointing directions, sometimes the anti-sun direction was not observed, but the oscillations around the leading azimuth of the gondola remained under control (see Fig. 1c). When the Sun illuminated the camera lens or strong solar reflections were present, such images were removed from the image analysis as overexposed. The number of the overexposed removed image accounted for about 2 % of the total number of images analyzed.

The TRANSAT balloon was launched from Esrange, northern Sweden (67.89° N, 21.08° E) at 18:57 UTC (20:57 LT) on 22 June 2024 and landed on Baffin Island, northern Canada, at 12:14 UTC (08:14 LT) on 26 June 2024. The total flight time was about 90 h (3.8 d), with an average horizontal speed of about 11 $\mathrm{m\,s^{-1}}$. The horizontal trajectory and altitude profiles of the TRANSAT mission are shown in Fig. 2.

2.3 Image processing

Prior to launch, all three Sony cameras underwent geometrical calibration on the ground using night-sky images containing reference stars. A second-order polynomial camera model was fitted by comparing theoretical and measured horizontal coordinates for over 200 identified reference stars. Six free coefficients describing focal length, image orientation, and optical distortion were determined. These coefficients were used to compute relative horizontal coordinates (elevation and azimuth angles relative to the center of the image) for every pixel of each camera.

Given the known position and orientation of the SONC imager within the gondola reference frame, provided by CNES, the absolute horizontal coordinates of all pixels were computed. Subsequently, a georeferencing procedure projected each pixel onto the Earth's surface, assuming a mean NLC altitude of 83 km. Details of the calibration, georeferencing, and error analysis are available in Dalin et al. (2015).

NLC identification was performed using both manual and automatic approaches. In the manual procedure, about 6200 images, suitable for scientific analysis, from the left camera (Fig. 1) were carefully examined to mark NLC presence or absence. A separate text file was created that in-

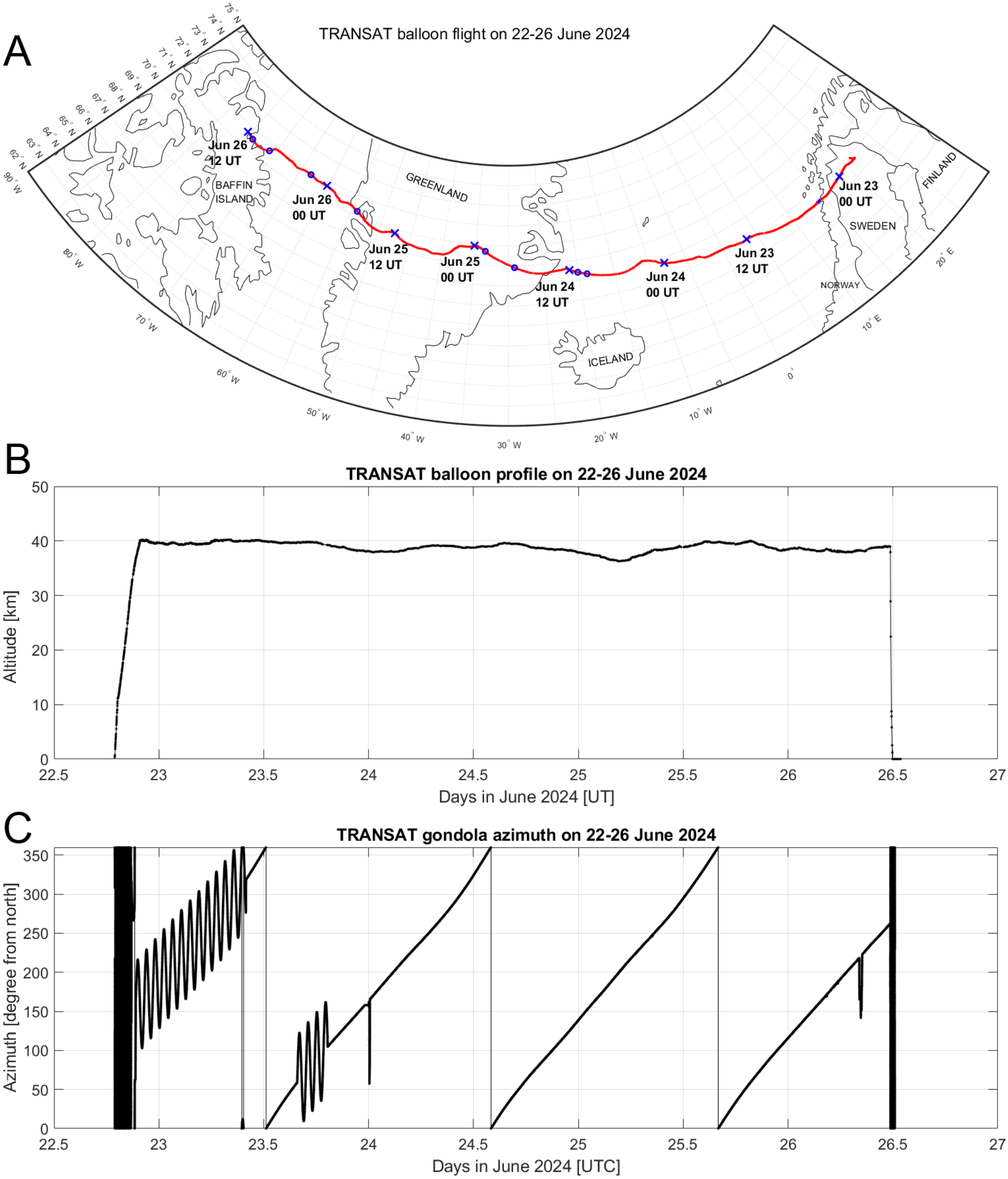

Figure 2. **(A)** Horizontal trajectory (the red line) of the TRANSAT balloon mission between 22 and 26 June 2024. The blue crosses mark the balloon's position every 12 h. The blue circles show the balloon's positions when no NLC were observed, see Sect. 4.1. **(B)** Altitude profile of the TRANSAT flight. **(C)** Azimuth of the optical axis of the left camera of the SONC imager due to the TRANSAT gondola rotation in the anti-sun direction for most of the flight.

dicates the cloud-free times during the TRANSAT flight. The number of images is 6200 because almost every image in a series of 5 images, taken in bracketing mode, was analyzed. A video sequence was then assembled to verify temporal continuity. This video, containing all images with synchronized flight parameters, timestamps and balloon coordinates, is available at the Harvard Dataverse repository (https://doi.org/10.7910/DVN/1PHRZU, Dalin, 2025a).

Automatic image processing involved several steps: (1) Background subtraction: a second-order polynomial fit was used to estimate the sky background along each vertical column of pixels, which was then subtracted to yield a residual brightness of each pixel. (2) Two-dimensional digital filtering: applied to a residual brightness to extract gravity-wave-like patterns on image (see Fig. 3b). To do this, we use zero-phase digital filtering by processing the residual brightness in forward and reverse directions along every vertical and horizontal line of the analyzed image. After filtering the data in the forward direction, the procedure reverses the filtered sequence and runs it back through the filter that provides a zero-phase distortion. A 4th-order Butterworth band-pass filter with a lower cutoff frequency of 0.0013 Hz and a higher cutoff frequency of 0.2 Hz is applied in this digital filtering procedure. (3) Wavelet analysis: a Morse analytic wavelet transform was applied to selected images to quantify horizontal wavelengths of identified wave patterns. An analyzed image was first projected onto Earth geographical coordinates (in km) prior to wavelet analysis. An example (Fig. 4) shows dominant horizontal wavelengths of about 30 and 40 km, which are frequently observed in NLC (Pautet et al., 2011; Demissie et al., 2014). In the present case, wave analysis was applied to the vertical slice (along the y axis) at the constant $X = 2200$ pixels of the filtered image shown in Fig. 3b. This example was chosen at random from 6200 images, but which demonstrates the NLC modulation due to gravity waves with the naked eye. Therefore, this analysis technique was applied to this image in order to estimate the horizontal scales of the wave packet in this case.

The spatial horizontal resolution of the pixels in the upper part of the projected image (close to the balloon) is about 21 m, of the pixels in the middle of the image is about 96 m, and of the pixels at the bottom of the projected image is about 1.2 km. In accordance with the Nyquist–Shannon sampling theorem, these values allow the study of NLC signals with horizontal scales greater than 42 m, 192 m and 2.4 km, respectively. Thus, medium- and large-scale gravity waves with horizontal wavelengths greater 50 km, small-scale gravity waves of 10–50 km, smaller-scale localized waves (billows or ripples) of 3–10 km can be analyzed throughout the image. Also, turbulent structures like vortex rings of 0.5–4 km in diameter can be studies in the upper and middle part of the image (Dalin et al., 2010; Pautet et al., 2011; Baumgarten and Fritts, 2014; Fritts et al., 2017, 2019).

(4) A keogram representation of a sequence of all analyzed images helps to identify the presence or absence of NLC as a function of time. A keogram is a slice of an image along a specific axis, and many such slices are put together as a function of time to produce brightness variations of an observed atmospheric phenomenon over time. A keogram is commonly used to demonstrate a presence or absence of aurora in all-sky images. In the present study, based on the manual careful inspection of 6200 images suitable for scientific analysis, we have selected horizontal pixel lines in the range of 3000–3400 pixels (counting along the y axis from the top of the image) at which NLC preferred to appear. These pixels correspond to a distance of about 315–583 km from the gondola position, when looking along the central line of the image. The image coordinates are present in Fig. 3b. These pixels were summed to produce an integrated brightness for every column between 3000 and 3400 pixels. The mean value and its standard deviation (SD) were then calculated for the given slice along the x axis of the image. We have separately estimated the mean brightness and its standard deviation for each image, thus the obtained values are independent of time and camera azimuth. Next, a selection rule was applied: brightness values greater than 1 SD of the mean were selected to classify the given slice as NLC present or absent. Then the keogram was created by putting together slices of about 6200 images (Fig. 5), demonstrating nearly continuous presence of NLC, that is discussed in detail in Sect. 4. This automatic keogram procedure fits well with the manual procedure (described above) in identifying the presence or absence of NLC as a function of time. The time intervals of the absence of NLC are indicated by red arrows that coincide with the manual and automatic procedure.

3 Ground-based and space complementary measurements

3.1 Lidar measurements

During the initial phase of the TRANSAT balloon flight, complementary lidar measurements were performed at Esrange (67.8° N, 21.1° E, Sweden) and Andøya (69.3° N, 16.0° E, Norway), with the aim to provide simultaneous and common volume (or in proximity) measurements of NLC layers above northern Scandinavia. At Esrange, we use a Rayleigh/Mie/Raman (RMR) backscatter lidar developed by the Bonn University to monitor aerosols in the troposphere, stratosphere and mesosphere as well as to determine temperature profiles in the aerosol-free part of the atmosphere (Blum and Fricke, 2005). The vertical and time resolution of the obtained measurements by the Esrange lidar is 150 m and 4.4 min, respectively. At Andøya, we use an RMR-lidar which has been operated as part of the Arctic Lidar Observatory for Middle Atmosphere Research (ALOMAR). Using measurements of the ALOMAR lidar one can study temperatures and winds in the middle atmosphere, aerosol layers in the stratosphere, polar stratospheric clouds in the

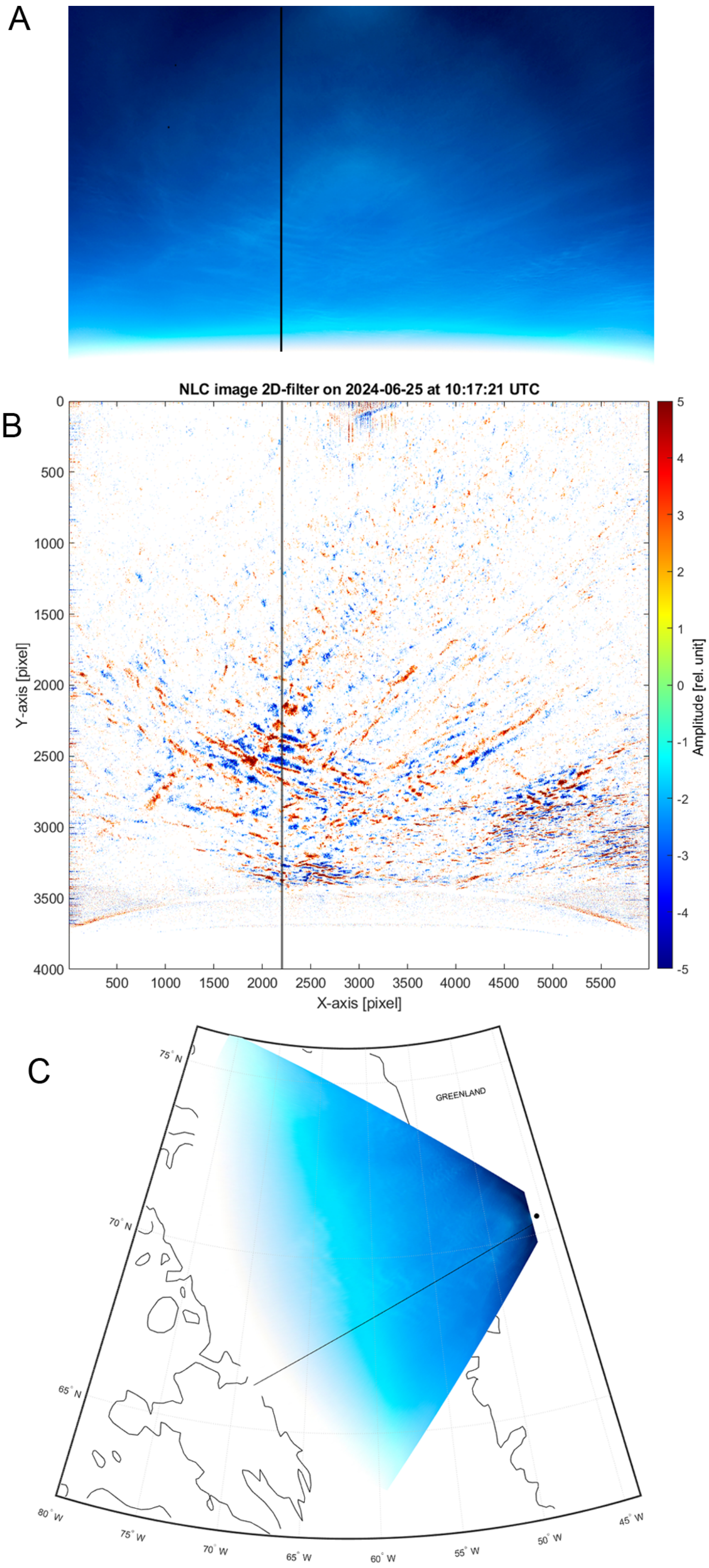

Figure 3. **(A)** Example of NLC image acquired at 10:17:21 UTC on 25 June 2024 during the TRANSAT balloon flight. **(B)** Two-dimensional Fourier-filtered version of **(A)**, highlighting residual brightness variations associated with NLC bands seen in the middle and the lower part of the image. **(C)** Projection of the NLC image shown on panel **(A)** onto the Earth's surface. The black dot is the position of the TRANSAT balloon. The black line shown in panels **(A)**, **(B)** and **(C)** shows the vertical slice at $X = 2200$ pixels where wavelet analysis was applied (see the text).

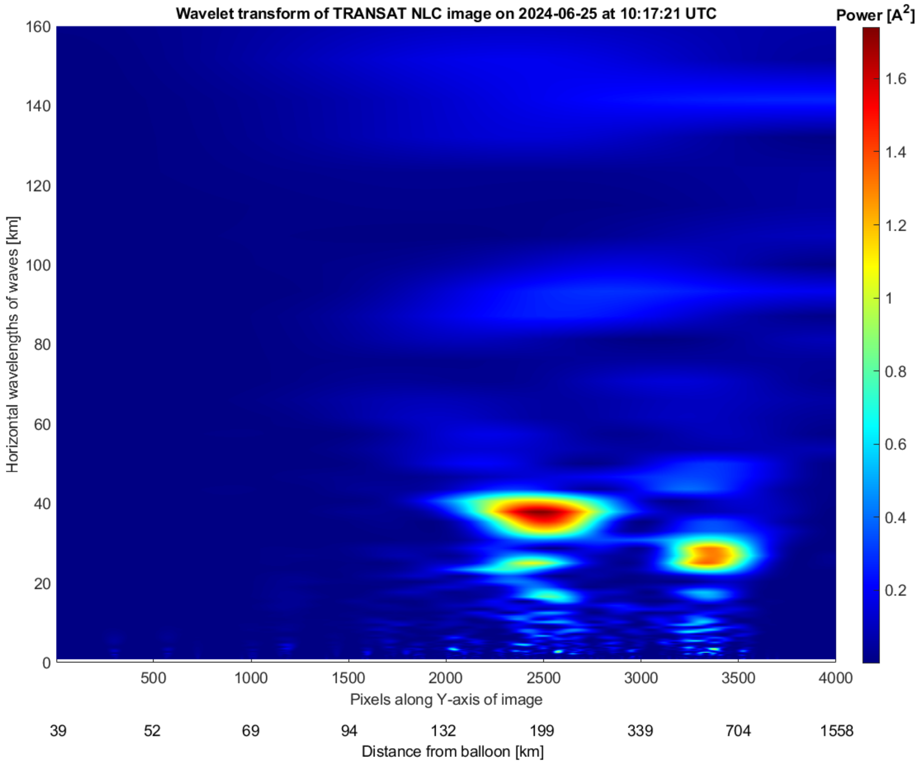

Figure 4. Example of a wavelet transform for the NLC image obtained at 10:17:21 UTC on 25 June 2024 during the TRANSAT flight. Gravity waves having prevailing horizontal scales of about 30 and 40 km are clearly seen as the red color code. Two different scales on the x axis are present: the upper scale is in pixels along the y axis at $X = 2200$ pixels of the image shown in Fig. 3a, the lower scale is the distance from the TRANSAT balloon in km.

lower stratosphere in winter and noctilucent clouds in the mesopause region in summer (Baumgarten, 2010). We use lidars backscattered signals from the 532 nm wavelength channel to measure NLC over Esrange and Andøya during the TRANSAT flight over northern Scandinavia. The vertical and time resolution of the obtained measurements by the ALOMAR lidar is 40 m and 30 s, respectively.

The results of the lidar measurements during the initial phase of the TRANSAT flight are shown in Fig. 6. The NLC layer is seen in both lidar measurements between 81 and 86 km altitude from 20:30 UTC on 22 June until 01:00 UTC on 23 June. Figure 6b shows raw Esrange lidar counts and Fig. 6c represents the filtered lidar data in the following way. All Esrange lidar data were averaged over a 600 m altitude interval and a 9 min time interval. Then the atmospheric background was estimated as the average value, and its standard deviation, of the lidar raw counts between 80 and 87 km for each time-averaged measurement. Counts exceeding 1.5 standard deviations from the average value were then selected. Figure 6c highlights the main features of the NLC layer seen in Fig. 6b. Between 20:00 and 22:00 UTC, the NLC layer lifted up from 84 to 86 km, then it sank to about 82 km between 22:00 UTC on 22 June and 01:00 UTC on 23 June as demonstrated by both lidars. After 01:00 UTC, Esrange lidar measurements become too noisy to distinguish the NLC signal from noise. Note that the ALOMAR lidar registered a double-layer NLC structure between 00:00 and 01:00 UTC. Another double-layer NLC structure will be discussed in Sect. 4. These height variations of the NLC layer are due to propagating atmospheric gravity waves. Note that it is a very rare case of conducting simultaneous lidar measurements of NLC layers at Andøya and Esrange (separated by ∼ 250 km) on both sides of the Scandinavian range. The ALOMAR lidar operated until 12:00 UTC on 23 June, continuously registering the enhanced NLC layer until about 09:30 UTC, with height variations between 81 and 84 km. The extended NLC field was registered by the SONC imager above northern Scandinavia (not shown in figure) starting from ∼ 22:00 UTC on 22 June 2024 and during the lidar measurements, thus continuously observing the NLC layer from the ground and stratosphere from evening hours on 22 June until morning hours on 23 June. Note that the comparison of the lidars measurements shown in Fig. 6 is qualitative because panels (A) and (B) are not shown in the same physical units.

Figure 7 illustrates the SONC images at 22:04:38 UTC on 22 June and at 09:34:32 UTC on 23 June, i.e., at the beginning and end of the NLC observations by the Esrange

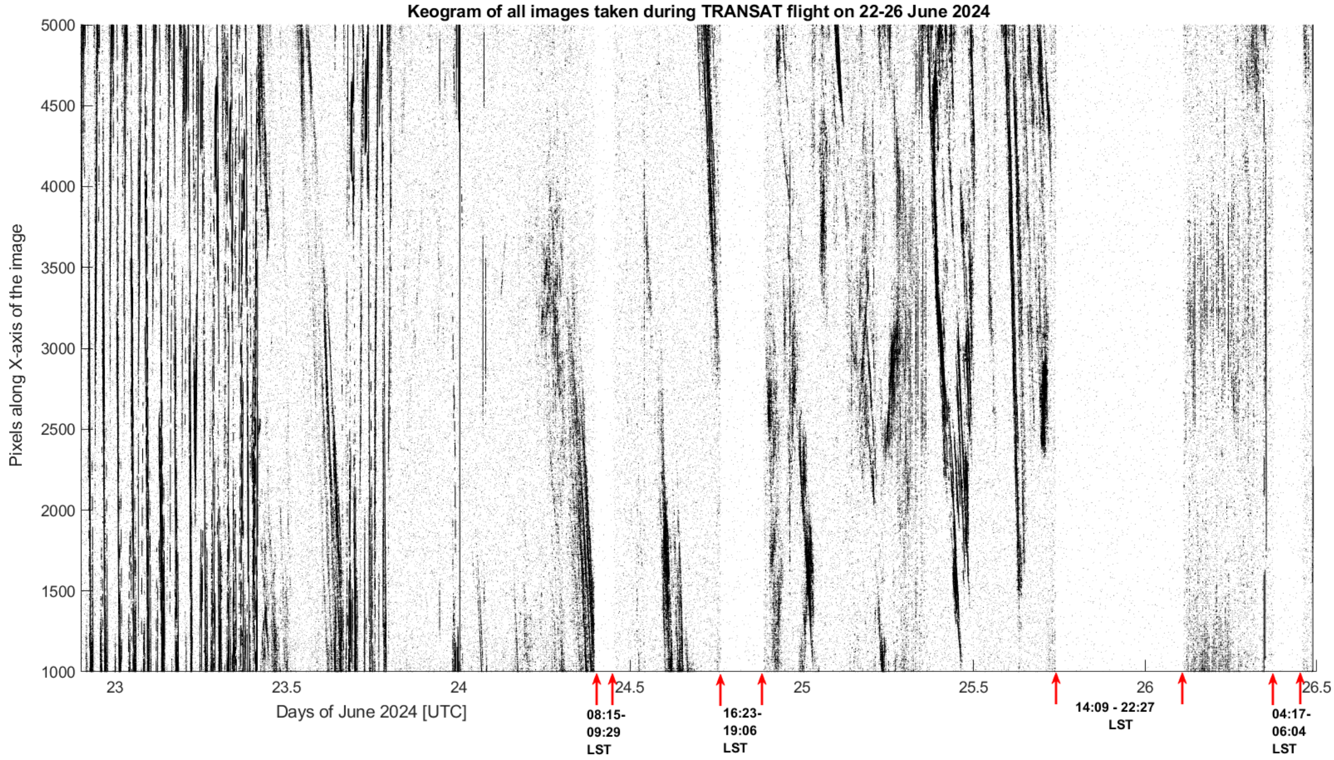

Figure 5. Keogram compiled from about 6200 images during the TRANSAT balloon flight on 22–26 June 2024. The red arrows mark four time intervals (white-grey areas) when NLC were absent. Corresponding local solar times (LST) are shown for four time intervals on the x axis. LST are calculated for the gondola position, but not for the observed NLC. The number of Y-pixels is equal to 401 for which the keogram was constructed.

and ALOMAR lidars. At the beginning of the lidars measurements the NLC observed by the SONC imager were located to the east of the lidars, but at the same latitude range (Fig. 7a). Later, the SONC imager slowly rotated in the antisolar direction, observing the east-south-west sector of the sky, and, thus, observations of NLC in the mesopause over the lidars were impossible. At the same time, at the very end of the ALOMAR lidar observations at about 09:30 UTC on 23 June, the SONC imager looked north-northeast and detected faint NLC at the very edge of the image frame directly over the ALOMAR lidar (Fig. 7b). At that time, NLC were between 81.6 and 82.0 km (Fig. 6a). Thus, lidar measurements can complement balloon-borne observations, providing information on vertical dynamics of the NLC layer observed from the stratosphere.

3.2 Space measurements

During the TRANSAT flight, measurements of PMC from space were also conducted with the MATS satellite. MATS (Mesospheric Airglow/Aerosol Tomography and Spectroscopy) is a Swedish satellite mission, launched in November 2022, designed to investigate polar mesospheric clouds, temperature regime and atmospheric gravity waves in the mesosphere (Gumbel et al., 2020). The MATS satellite utilizes airglow emissions coming from excited molecular oxygen in the near infrared range of the spectrum (760–780 nm, the O_2 (0-0) A-band) as well as scattered light from PMC in the ultraviolet (270 and 340 nm). The primary scientific instrument on-board the satellite is the limb imager, a telescope with six wavelength channels that continuously captures images of the atmospheric limb with a field of view of about 40 km in the vertical and 250 km across track at the tangent point. The horizontal and vertical resolution of MATS limb images is 5.7 km and 290 m, respectively. The horizontal resolution is consistent with AIM/CIPS images (Randall et al., 2017) and the vertical resolution of 290 m should be considered high for satellite missions. Using a tomographic analysis of acquired MATS images, one can reconstruct waves in three dimensions and provide 3-dimensional fields of airglow, PMC properties and temperature (Megner et al., 2025).

Figure 8 demonstrates an example of MATS images in the UV channel 1 at 270 nm taken at 10:48:08 UTC on 25 June 2024. This measurement was done at the tangent point in the mesopause close to the west coast of Greenland as illustrated in Fig. 8d. One can clearly see the presence of the PMC layer in Fig. 8c as the bright yellow band on the atmospheric limb between 80 and 85 km tangent altitude.

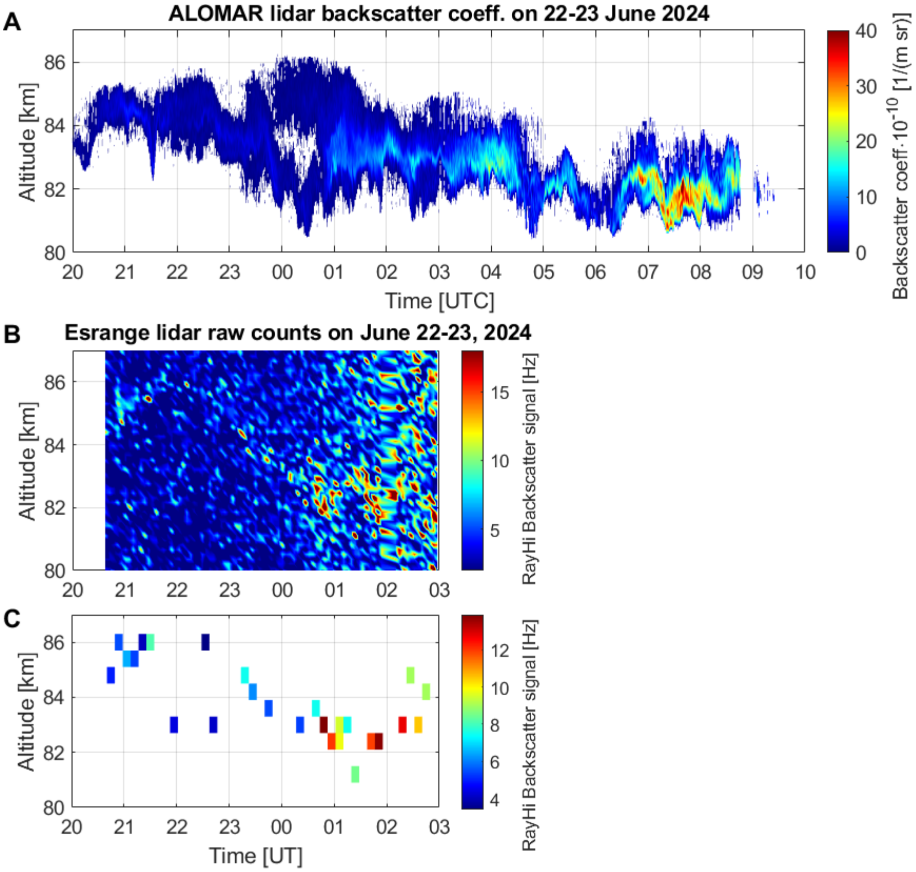

Figure 6. Lidar measurements at Andøya, Norway **(A)** and Esrange, Sweden **(B)** during the initial phase of the TRANSAT balloon flight on 22–23 June 2024. **(C)** Filtered Esrange lidar data averaged over a 600 m altitude interval and a 9 min time interval (see the text).

The time and location of the PMC by MATS agree very well (time difference of 6 s) with the NLC observation obtained from the TRANSAT balloon, with the MATS tangent point being in the field of view of the SONC imager as seen in Fig. 8d. Such simultaneous common-volume observation of NLC from the stratosphere and space was made for the second time; the first one was made by the PMC Turbo stratospheric flight and the AIM satellite in July 2018 (Fritts et al., 2019). But in the present study this was done for the first time when such a large-scale NLC/PMC field (extending at least 1500 km from north to south) was seen from the stratosphere and from space based on the limb-viewing observation using the MATS satellite. Note that MATS also detected NLC in the next orbit over Greenland and in field of view of the SONC imager at 12:22:16 UTC on 23 June (not shown in figure). In the present study, we do not aim to completely compare all possible NLC observations from the stratosphere and the MATS satellite, but to demonstrate the fundamental possibility of such observations in one figure only. Thus, MATS observed an extended PMC layer in a large volume of the mesopause at least over Greenland, Baffin Bay and Baffin Island. Part of this large-scale NLC field was registered from the stratosphere by the SONC imager shown in Fig. 8a. Figure 8b demonstrates a 2D-filtered image with a second-order polynomial removed from the original image (see Sect. 2.3), which shows NLC modulations due to gravity waves of various scales throughout the lower part of the image. At the same time, images taken from the stratosphere have much higher spatial resolution, showing small- and medium-scale wave dynamics (including smaller gravity waves and turbulent structures) that MATS cannot resolve using the limb-viewing geometry. Thus, studies of spatial-temporal variability of NLC/PMC can be carried out simultaneously from the stratosphere and space, complementing each other.

4 Results and Discussion

4.1 Nearly continuous observations of NLC

The first scientific result is the nearly continuous presence of mesospheric clouds in the observed latitude range of 60–75° N during 3.8 d of the TRANSAT balloon flight. In total, there were four intervals of NLC disappearances as shown by the blue circles in Fig. 2a and by the red arrows in Fig. 5. These events occurred on 23 June at 09:30–

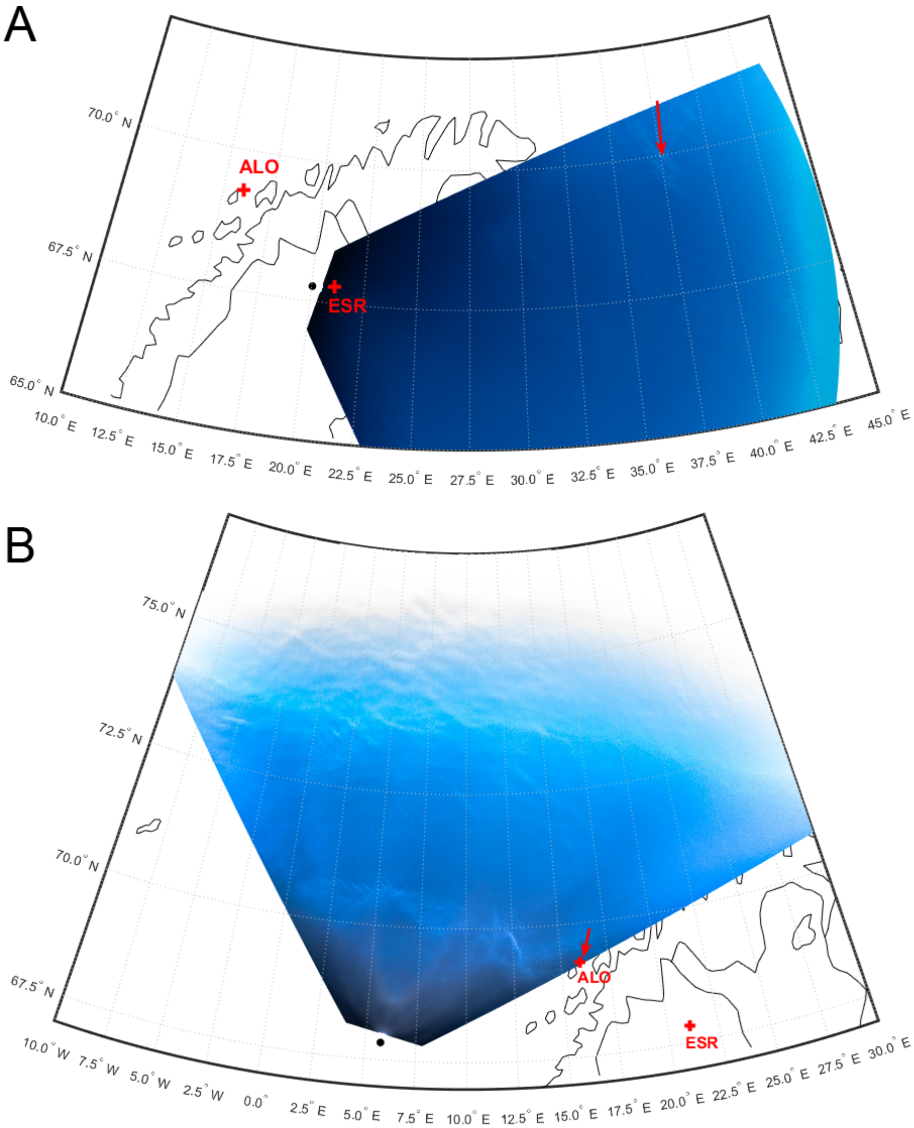

Figure 7. Projection of two SONC images on the Earth's surface at 22:04:38 UTC on 22 June 2024 **(A)** and at 09:34:32 UTC on 23 June 2024 **(B)** during the TRANSAT balloon flight. The black dot denotes the balloon position. The red crosses are the position of the ALOMAR (ALO) and Esrange (ESR) lidars. The red arrows show the locations of NLC.

10:50 UTC on 23 June, at 18:20–21:20 UTC on 24 June, at 17:45–02:40 UTC on 25–26 June, and at 09:00–11:00 UTC on 26 June. Outside these intervals, NLC were continuously observed, often with varying brightness and wave modulation.

These NLC disappearances are not related to local solar time (see four local solar time intervals on the *x* axis in Fig. 5). That is, these NLC interruptions were of a rather spontaneous nature and were not related to solar thermal tides, which are regular atmospheric variations. Indeed, Fritts et al. (2019) demonstrated more or less regular NLC disappearances in the evening (18:00–24:00 LST) and morning hours (06:00–12:00 LST), observed during the PMC Turbo balloon flight from Sweden to Canada in July 2018. The authors associated this with solar semidiurnal and diurnal thermal tides in the polar summer mesopause, the amplitudes of which reach 10–20 K, which is comparable to ones by gravity waves in the mesopause region (Rapp et al., 2002). It should be noted that this result was obtained on the basis of lidar measurements on the PMC Turbo balloon, that is, obtained with a very small field of view of a few meters in the mesopause. Therefore, for such a small volume of the mesopause one can expect the dominant influence of large-scale waves such as solar tides. Note that continuous lidar observations at 69° N demonstrate strong NLC diurnal variations due to solar tides, with a maximum occurrence frequency of about 65 % in the morning hours and a minimum of about 35 % around noon (Fiedler et al., 2011). In the case

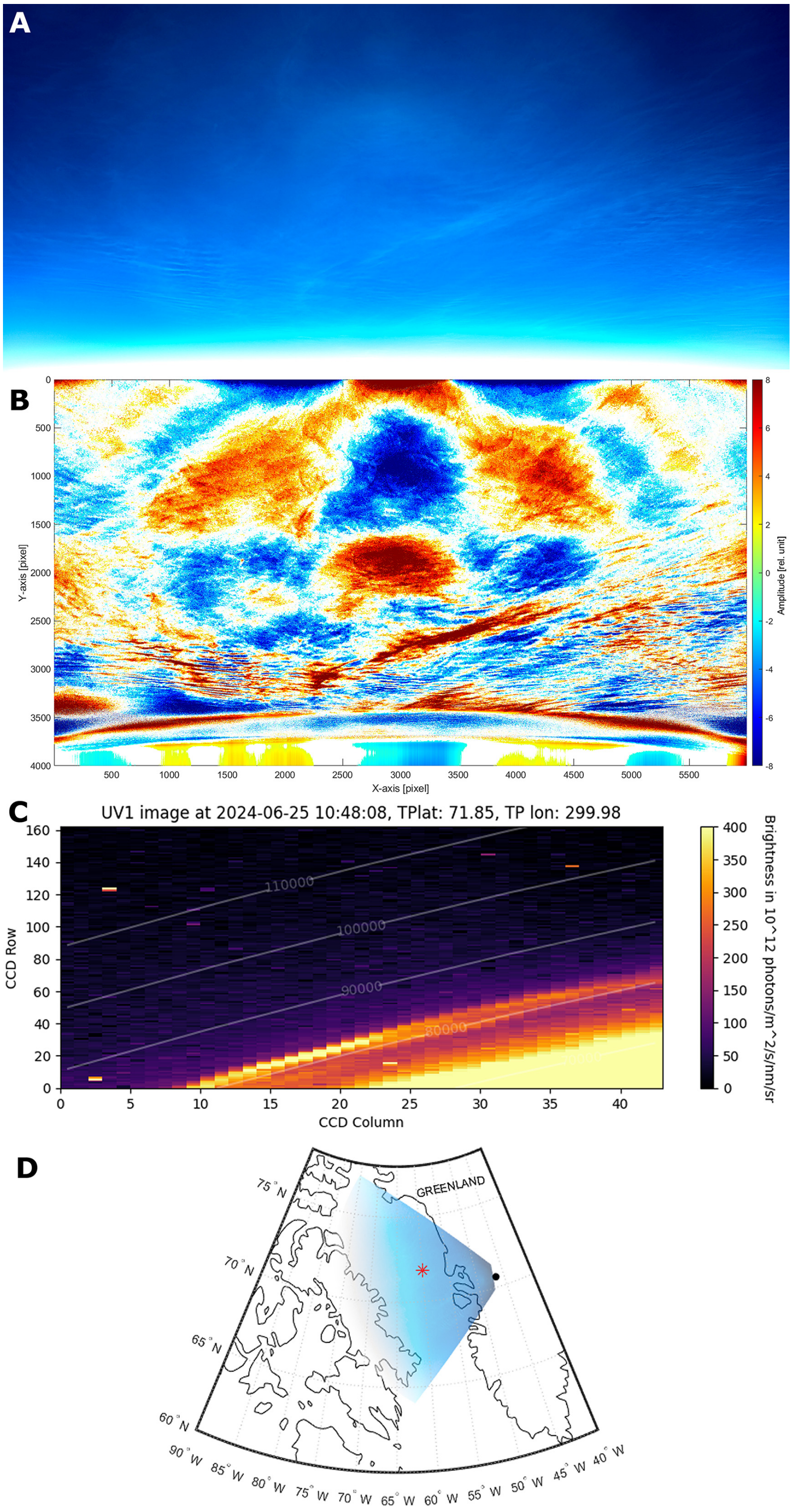

Figure 8. Example of NLC measurements obtained from the stratosphere and space on 25 June 2024 during the TRANSAT balloon flight. **(A)** Image, taken by the SONC imager at 10:48:02 UTC, shows the extended NLC field covering almost the whole image area. **(B)** 2D-filtered image with a second-order polynomial removed from the original image shown in **(A)** (see the text). **(C)** Image, taken by the MATS satellite at 10:48:08 UTC, illustrate part of the atmospheric limb, with the bright yellow PMC layer seen between 80 and 85 km. Data are shown for the UV channel 1 at 270 nm. **(D)** Projection of the NLC image shown on panel **(A)** onto the Earth's surface. The black dot is the position of the TRANSAT balloon, the red asterisk marks the MATS tangent point which is in the field of view of the SONC imager.

of the TRANSAT balloon flight NLC observations were carried out on large scales of about 1000–1500 km at a time. At such large scales, not only solar tides manifest themselves but also propagating gravity waves of various scales from 1 to 1000 km. Indeed, a typical picture seen from the stratosphere was that we saw a disappearance of NLC in one area of the mesopause (for example, in the eastern part), but simultaneous appearance of other NLC in another part of the mesopause (for example, in the western part). In other words, large-scale NLC fields were generally represented by numerous wavy patterns of sporadic nature. One can assume that gravity waves, continuously coming from the lower atmosphere, form a new NLC and/or modulate an existing NLC layer in different parts of the mesopause (as observed in the present experiment), thereby dominating solar thermal tides on large scales. At the same time, we should note that this result was obtained on the basis of a single 3.8 d flight and a limited range of latitudes (60–75° N) and longitudes (45° E–95° W). That is why the present case study cannot claim to be a general statement about the relative importance of solar tides compared to gravity waves.

4.2 A case study of the NLC disappearance

The second result is connected to the disappearance of NLC at 18:20–21:20 UTC (16:23–19:06 LST) on 24 June 2024 (Fig. 5). This NLC disappearance was observed over the Atlantic Ocean near the east coast of Greenland and over Iceland as demonstrated in Fig. 9.

We have tried to find out the reason for this NLC disappearance. For this data of the Aura/MLS temperature and water vapor measurements have been used to obtain a comprehensive picture of the mesopause environment in the region of interest. Aura/MLS temperature and water vapor measurements of ver.5.0 and level 2 data quality were obtained from the NASA public website: https://acdisc.gesdisc.eosdis.nasa.gov/data/Aura_MLS_Level2/ (last access: 27 April 2026). According to the Aura/MLS data quality and description document (version 5.0x level 2 and 3), for Aura/MLS temperature measurements, the vertical resolution in the mesopause region is 11 km at 0.01 hPa ($\sim$ 80 km) and 12 km at 0.001 hPa ($\sim$ 90 km). The horizontal resolution (along track) is $\sim$ 250 km at 0.01 hPa and $\sim$ 280 km at 0.001 hPa. The pressure range recommended for scientific use is from 261 hPa ($\sim$ 10 km) to 0.00046 hPa ($\sim$ 93 km). Typical precisions for individual Aura/MLS temperature profiles at this altitude range are ±3.4–3.6 K. For Aura/MLS water vapor measurements, the vertical resolution is 8.8 km at 0.01 hPa and 10.3 km at 0.002 hPa. The horizontal resolution is $\sim$ 725 km at 0.01 hPa and $\sim$ 350 km at 0.002 hPa. The pressure range recommended for scientific use is from 316 to 0.001 hPa. Typical precisions for individual Aura/MLS water vapor profiles are 55 % at 0.01 hPa and 450 % at 0.001 hPa. The description on the MLS temperature product and its validation can be found in Froidevaux et al. (2006) and Schwartz et al. (2008). The validation of water vapor data is described in detail by Read et al. (2007) and Lambert et al. (2007). The frost point temperature in the mesopause was calculated using Aura/MLS water vapor data based on thermodynamics of the vapor pressure of ice (Murphy and Koop, 2005).

The results are shown in Fig. 10 demonstrating the following peculiar feature. A prominent localized warm area in the mesopause region at the pressure levels of 0.0022 hPa (about 86 km geometrical height) and 0.0046 hPa (about 83 km) was present between Greenland and Scandinavia, with temperatures 20–30 K higher than those in the adjacent mesopause regions at 0.0022 hPa. The location of this warm spot coincides well with the position of the mesopause visible from the TRANSAT balloon when no NLC were seen (Fig. 9). The right column in Fig. 10 shows the differences between the actual temperature measurements and the frost point temperature as calculated using Aura/MLS water vapor measurements, with positive temperature differences being as much as 10–15 K in the center of this warm spot. We double-checked all the Aura/MLS data (temperature and water vapor) which show good quality data suitable for scientific analysis and we could not find any error in these data.

In Fig. 10 (especially in plots for the 0.0046 hPa level), one can note that the warm local region at high latitudes was an extension of a warm vast area located at mid-latitudes. That is, one can assume that this local warm region was caused by a jet of warm air mass from middle latitudes to high latitudes. To test this hypothesis, we apply the Japanese Atmospheric General circulation model for Upper Atmosphere Research Data Assimilation System (JAGUAR-DAS), which is a data assimilation system for the whole neutral atmosphere (Koshin et al., 2020, 2022). Specifically, JAGUAR-DAS Whole neutral Atmosphere Reanalysis (JAWARA) has been considered in the present study. JAWARA is a long-period reanalysis, starting from September 2004, which covers the altitude range from the surface to the lower thermosphere ($\sim$ 110 km). The vertical resolution of JAWARA data in the mesopause region between 80 and 90 km is about 0.7 km. JAWARA outputs, distributed on a horizontal grid spacing of 2.81°, include the following hourly data: temperature, zonal, meridional and vertical wind velocities, geopotential height, temperature tendency due to diabatic heating, zonal and meridional forcing from the GW parameterization (Koshin et al., 2025). Note that JAWARA assimilates MLS temperature, meaning that the temperature fields in MLS and JAWARA are not fully independent and the mutual agreement might be expected because of the data assimilation.

JAWARA temperature and neutral wind data in the mesopause region are shown on 24 June 2024 in Fig. 11, demonstrating the following features. The warm localized spot was present between Greenland and Scandinavia, and it was most pronounced at 0.0042 hPa, $\sim$ 83 km, (lower plots), which agrees well with the position of the warm spot repre-

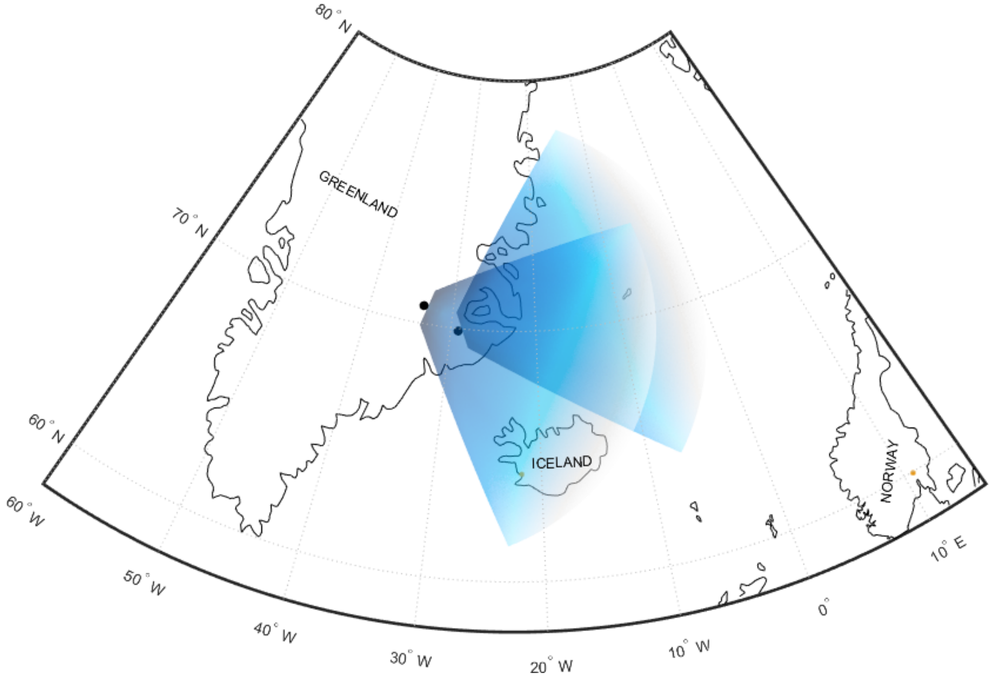

Figure 9. Projection of the field of view of the SONC camera on the Earth's surface at 18:20 UTC (16:23 LST) and 21:20 UTC (19:06 LST) on 24 June 2024, when no NLC were observed from the stratosphere. The black dots mark the position of the TRANSAT balloon.

sented by Aura/MLS. At the same time, wind velocity vectors show that the local wind jet was formed, which moved from middle to high latitudes in the region with this warm spot. Thus, this warm spot in the mesopause was caused by the intrusion of a warm air mass from the middle to high latitudes between Greenland and Scandinavia. This warm spot induced sublimation of ice particles in the mesopause, which caused NLC to disappear during the TRANSAT balloon flight over the North Atlantic and the east coast of Greenland in the evening of 24 June 2024. The mechanism of this air intrusion from middle to high latitudes is beyond the scope of the present paper.

In general, the relationship between NLC occurrence and ambient mesopause temperature is known. Berger and von Zahn (2002), using model studies with a 3-D general circulation model of the middle atmosphere (COMMA/IAP), demonstrated that the saturation ratio $S = 1$ closely coincides with a temperature of 147 K at 83 km altitude at any latitude poleward of 65° N. If the air is supersaturated ($S > 1$), this condition allows ice particles to exist in the summer mesopause region between 83 and 93 km, depending on latitude. A similar experimental result on the mesopause temperature was found by Dalin et al. (2011), who analyzed Aura/MLS temperatures and NLC occurrences observed from the ground around the globe. The authors found that MLS temperatures around the mesopause control the NLC climatology, i.e., a drop in temperature below the frost point temperature in June corresponds to the beginning of the NLC season, and an increase in temperature above the frost point temperature in August determines the end of the NLC season. The mesopause frost point temperature was estimated to be in the range of 145 to 147 K, with water vapor contents varying between 3.5 and 6.0 ppmv. Hervig et al. (2015), analyzing NLC observations from space using AIM/SOFIE, found that NLC variations are dominated by the mesopause temperature, but a combination of temperature and water vapor content provides the best description of ice water content in the Northern Hemisphere mesopause. At high latitudes, Fiedler et al. (2011) found a strong anticorrelation (−0.96) between LIMA model temperatures and diurnal NLC occurrences above ALOMAR (69° N). At middle latitudes, Gerding et al. (2013) found anticorrelations in the range of −0.76 to −0.85 (depending on altitude) between the NLC occurrence rate and mesopause temperature using lidar measurements at Kühlungsborn (54° N). We should note that the present case study demonstrates not only the well-known link between increased temperature and NLC absence, but more importantly, the intrusion of a warm air mass from the middle to high latitudes in the mesopause region. The latter phenomenon is poorly studied and rarely found in the literature.

4.3 A double-layer structure in NLC

The third early result addresses a double-layer event in NLC observed over Greenland on 25 June 2024. The reader is recommended to look at the video of NLC image sequence at 05:08–06:49 UTC (02:35–04:08 LST) on 25 June (https://doi.org/10.7910/DVN/AKJK4P, Dalin,

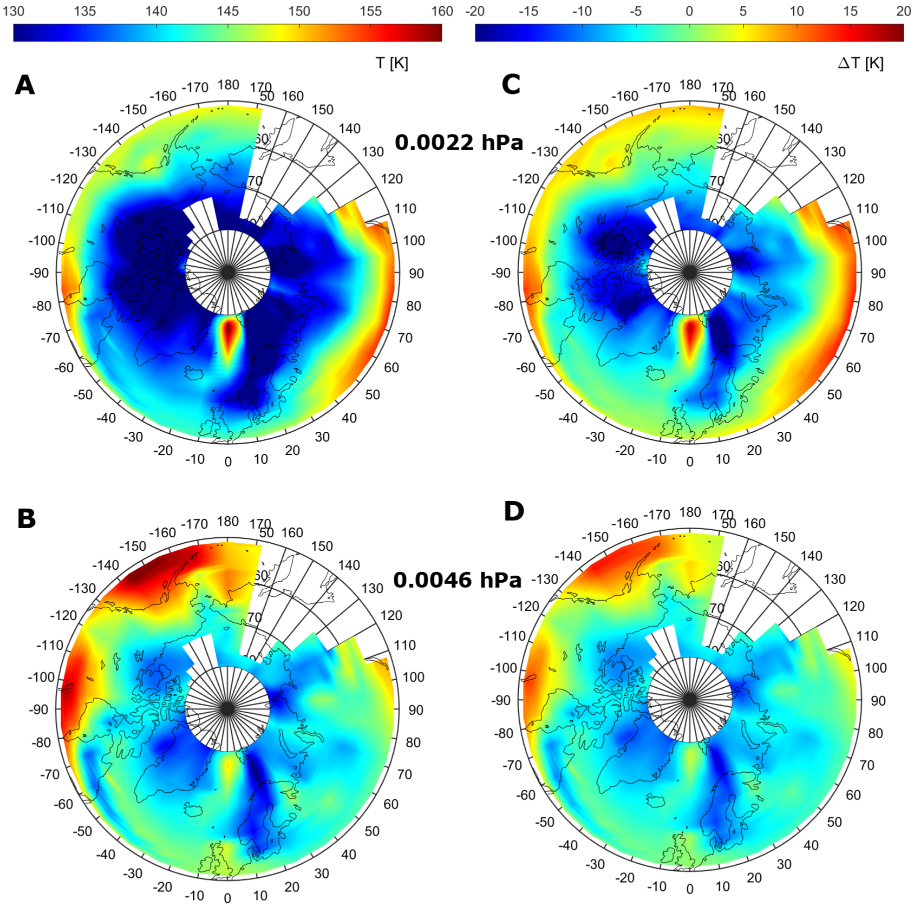

Figure 10. **(A)** Aura/MLS temperature measurements at the pressure level of 0.0022 hPa (∼ 86 km) and **(B)** at 0.0046 hPa (∼ 83 km) on 24 June 2024. Differences between the temperature and the frost point temperature as estimated based on Aura/MLS water vapor measurements at 0.0022 hPa **(C)** and 0.0046 hPa **(D)**, see the text.

2025b). One can see at least two NLC layers moving in opposite directions: one cloud layer visually moved approximately from the top to the bottom of the image frame, whereas another cloud layer moved in the opposite direction from the bottom to the top. Double-layer and multiple-layer structures in NLC/PMC have been previously observed and modeled in a number of studies (Baumgarten et al., 2012; Dubinskii and Popel, 2012; Kaifler et al., 2013; Gao et al., 2017; Li et al., 2016).

We have carefully estimated speeds and directions of seven individual NLC points in each of these two different layers. NLC point trace analysis was applied to the original (unfiltered and unprojected) images. After completing the trace analysis, the estimation of NLC velocities (speeds and directions) was performed on projected images. The results of this analysis are as follows. For the NLC layer visually moving from the bottom to the top, the average NLC speed was about 28 $\mathrm{m\,s^{-1}}$, with the average azimuth of about 18° (counting clockwise from the north). For the NLC layer moving from the top to the bottom, the average NLC speed was about 60 $\mathrm{m\,s^{-1}}$, with the average azimuth of about 193°. These statistical results are summarized in Table 1 as well as shown in Fig. 12, demonstrating NLC velocity vectors (green and yellow arrows) estimated for the two different layers. Note that we have taken into account the velocity vector of the TRANSAT flight (zonal and meridional speed was -10.5 and $-7.1\,\mathrm{m\,s^{-1}}$, respectively) when calculating these NLC wind velocities vectors. To calculate NLC speeds, the average height of the entire cloud layer was chosen as 83 km. Uncertainty in the height of the NLC layers between 82 and 86 km gives an error of 3 %–4 % of the average NLC speed.

It can be assumed that different movements of the two NLC layers were caused by different wind systems located at different heights in the mesopause region. We cannot measure the heights of the different NLC layers but we can consider a model simulation to check this assumption. We utilize JAWARA zonal and meridional wind data in the mesopause region taken at 06:00 UTC on 25 June 2024, i.e., when and where different motions of the NLC were observed.

JAWARA wind data are shown in Fig. 12 by the vector field as well as by the absolute wind speed (color code). Panel (A) represents JAWARA wind data at the pressure

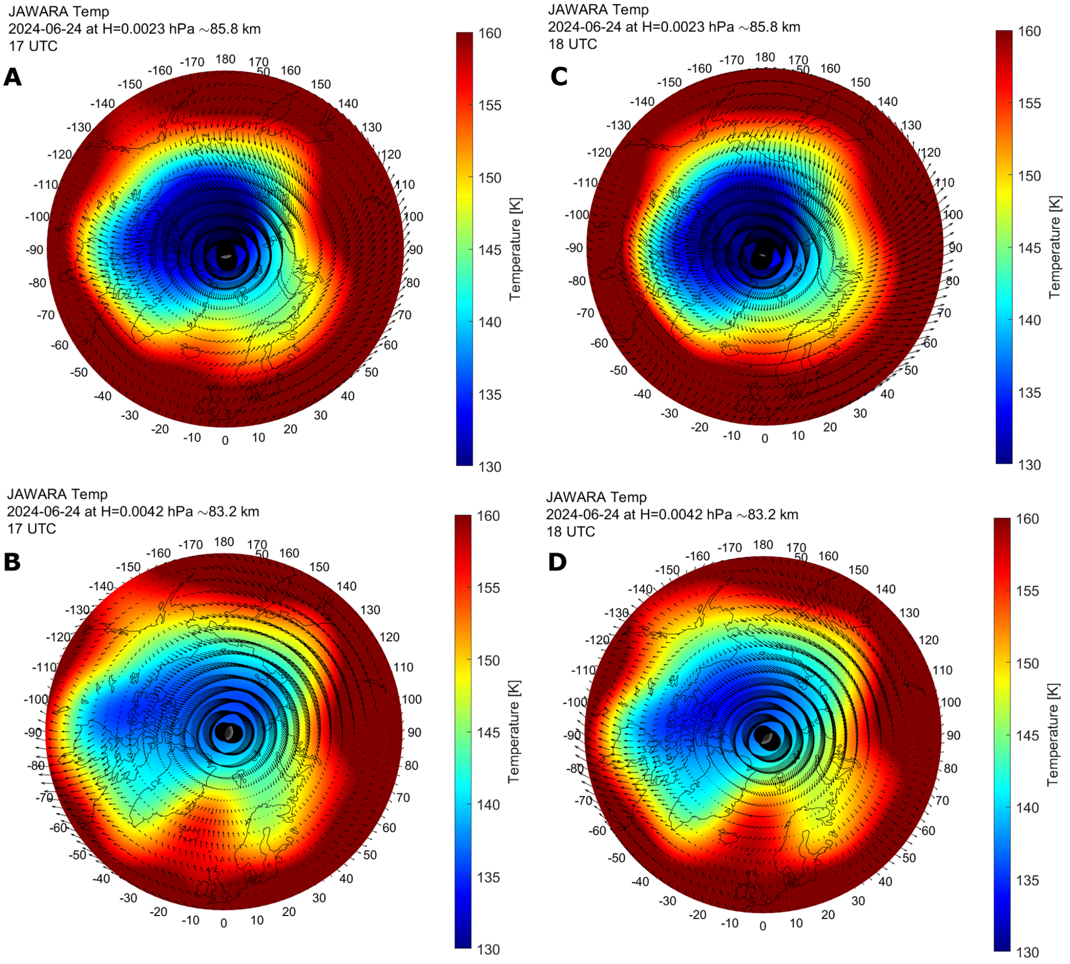

Figure 11. JAWARA model temperature (color code) and neutral wind velocity vectors (arrows) on 24 June 2024. The data are shown at the pressure level of 0.0023 hPa **(A, C)** and at 0.0042 hPa **(B, D)**, and at 17:00 UTC **(A, B)** and at 18:00 UTC **(C, D)**.

Table 1. Statistical parameters of the movement of two different layers observed in NLC during the TRANSAT balloon flight on 25 June 2024. For comparison, wind data from the JAWARA model are shown. Uncertainties represent one standard deviation.

Two NLC layers oppositely moved in image frame	NLC speed ($\mathrm{m\,s^{-1}}$)	NLC azimuth (degree from north)	JAWARA wind speed ($\mathrm{m\,s^{-1}}$)	JAWARA wind azimuth (degree from north)
From bottom to top	27.8 ± 10.0	18.2 ± 8.2	21.0 ± 3.7 at 0.0042 hPa	13.0 ± 12.0 at 0.0042 hPa
From top to bottom	60.5 ± 11.3	192.5 ± 2.2	56.1 ± 2.5 at 0.0017 hPa	188.0 ± 4.3 at 0.0017 hPa

level of 0.0042 hPa (~ 82.9 km) above Greenland and seven NLC velocity vectors (green arrows) observed in the NLC layer which was moving in the NNE direction (visually from the bottom to the top). The average wind speed was about 21 $\mathrm{m\,s^{-1}}$ in the direction of 13° (counting clockwise from the north) in the vicinity of the observed NLC. Panel (B) illustrates JAWARA wind data at the pressure level of 0.0017 hPa (~ 86.8 km). One can see about the opposite direction (to SSW) of the model wind field to that shown on panel (A). The average JAWARA wind speed was about 56 $\mathrm{m\,s^{-1}}$, with the average azimuth of 188°, in the vicinity of the observed NLC. Seven NLC velocity vector are shown by the yellow arrows which have about the same speed and the direction of motion. All these statistical data are summarized in Table 1, which demonstrate good agreement between the measured NLC and JAWARA wind velocities both in the absolute value and in the propagation direction, taking into account their uncertainties. Note that the JAWARA model has a low horizontal spatial resolution (2.81° or ~ 310 km in latitude and ~ 113 km in longitude in the analyzed space domain over Greenland) and cannot reproduce wave dynamics due to small-scale gravity waves. However, in this particular

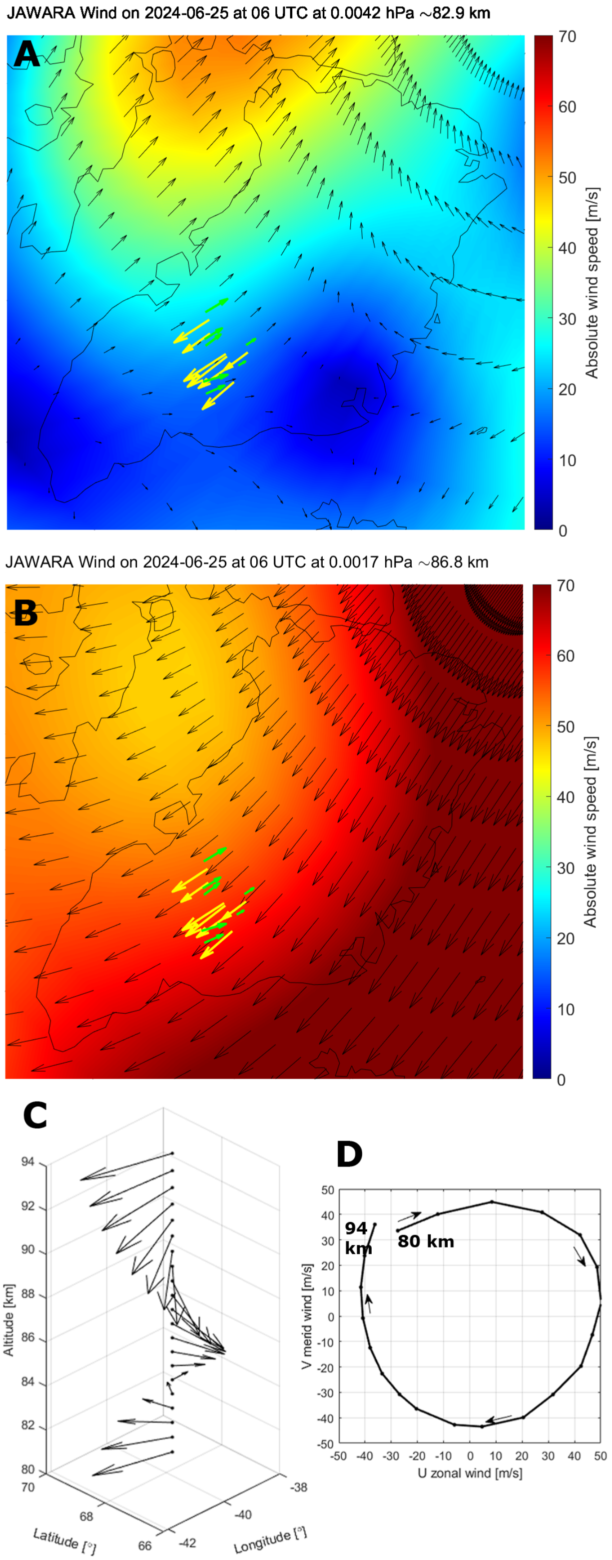

Figure 12. JAWARA wind data (thin black arrows) at the pressure level of 0.0042 hPa, ~ 82.9 km **(A)** and at the pressure level of 0.0017 hPa, ~ 86.8 km **(B)** at 06:00 UTC on 25 June 2024. The color code is the absolute horizontal wind speed. The green and yellow arrows show velocities of NLC moving in opposite directions (see the text). **(C)** JAWARA wind velocity vector selected for a specific location (68.4° N, 39.4° W) as a function of altitude between 80 and 94 km. **(D)** Hodograph of disturbances of the horizontal wind velocity vector between 80 and 94 km. The thin arrows show the direction (clockwise rotation) of wind velocity disturbances with altitude.

case, the JAWARA model does correspond well to the observed motions of the two different NLC layers.

Panel (C) of Fig. 12 shows the JAWARA wind velocity vector as a function of altitude for a specific point in the vicinity of the observed NLC. The cyclic rotation of the wind velocity vector is clearly seen between 80 and 94 km altitude, i.e., there was a circular rotation of the wind vector along the azimuth of 360°. Panel (D) illustrates the corresponding hodograph of the tip of the horizontal wind vector with the subtracted mean velocity values (-33 and $-18\,\mathrm{m\,s^{-1}}$ for the zonal and meridional wind component, respectively) between 80 and 94 km, that is, perturbations of the horizontal wind velocity. It is well known that a gravity wave induces horizontal wind variations rotating, in general, elliptically with height, and hodograph analysis is commonly used to derive gravity wave parameters (Gossard and Hooke, 1975; Eckermann, 1996 and references therein). In the present case, the hodograph has an almost circular form, implying near circular polarization ($P \approx 0$). Perturbations of the horizontal wind are of 45–50 $\mathrm{m\,s^{-1}}$, and the perturbation vector has a clockwise rotation with increasing height which means that the group velocity of this particular gravity wave was propagating upward (phase velocity was downward). Such an inertia-gravity wave could indeed generate winds in different directions in the given volume of the mesopause, forming a multiple-layer structure from a single NLC layer. The inertia-gravity wave interpretation is a plausible scenario which is consistent with JAWARA winds and NLC motions. At the same time, it should be noted that the background wind in the mesopause region abruptly changes its speed and direction with altitude in summer (Portnyagin and Solovjova, 2000; Conte et al., 2025). Therefore, other mechanisms such as the vertical displacement of the NLC layer by gravity waves, may provide the observed different NLC motions.

It is important to note the following. The clockwise wind rotation with altitude by JAWARA was the opposite of that found by Conte et al. (2025), who have analyzed long-term meteor radar measurements in the mesopause region at high latitudes over northern Norway. The authors have obtained the counter-clockwise rotation of the mean wind speed with altitude in the summer time. The same effect of the wind rotation with altitude is predicted by the global empirical wind model for the upper mesosphere/lower thermosphere (Portnyagin and Solovjova, 2000). In this present case, the clockwise rotation of the wind speed indicates the dominance of the inertia-gravity wave over the mean wind rotation speed in the space-time domain under consideration. Also, we should note that even without inertia-gravity waves, winds in the mesopause region can rotate with altitude (Ekman spiral) under the action of the Ekman-type mechanism involving Coriolis force and turbulent viscosity (Chkhetiani and Shalimov, 2010, 2022).

5 Conclusions

Observations of noctilucent clouds were performed from the stratosphere during the TRANSAT transatlantic long-duration balloon flight between Sweden and Canada on 22–26 June 2024. NLC were observed with the SONC imager composed of three high-resolution SONY α7 Mark III cameras, stabilized on the TRANSAT gondola. NLC cannot be detected by an imager from the ground during the midnight Sun season due to strong background scattering in the lower atmosphere. However, an observation from the stratosphere can detect NLC during 24 h. Stratospheric measurements offer a view of mesospheric cloud dynamics on small- and large-scales, bridging the observational gap between ground-based and satellite platforms. The main results of this study can be summarized as follows:

1. One wide-angle camera was completely operational during the whole flight for 3.8 d, taking a total of 40 000 images, of which about 6200 images are suitable for scientific analysis.

2. NLC were detected nearly continuously during the whole flight, showing a strong variability in space and time. The dominant role of solar thermal tides in the summer mesopause decreases when NLC are observed on large scales of about 1500 km. At such scales, gravity waves of various scales from 1 to several hundred km play the largest role, evolving and modulating NLC layers in different regions of the polar mesopause. Note that this result was obtained on the basis of a single 3.8 d flight and a limited range of latitudes (60–75° N) and longitudes (45° E–95° W). Thus, the present case study cannot claim to be a general statement about the relative importance of solar tides compared to gravity waves.

3. Ground-based support of the TRANSAT balloon campaign was represented by two lidars located at Esrange and Andoya. Both lidars registered NLC at the time of the initial phase of the balloon flight over northern Scandinavia. The NLC layered was continuous from 20:00 UTC on 22 June until 09:00 UTC on 23 June, modulated in height between 81 and 86 km, and showing a double-layer structure.

4. The same mesospheric cloud layer was recorded from the stratosphere and space around noon on 25 June 2024. Such a simultaneous common-volume NLC detection was carried out, for the first time, using a limb-geometry by the MATS satellite. The extended cloud layer was observed over at least Greenland, Baffin Bay and Baffin Island, with part of this layer registered from the stratosphere over the west coast of Greenland and Baffin Bay. Images from the stratosphere showed complex wave dynamics, with interference of small-scale waves and turbulent regions below what MATS can partly resolve.

5. Gravity waves had characteristic horizontal wavelengths of 30–40 km for the case study considered in the mesopause over Greenland on 25 June 2024.

6. One peculiar case of the NLC disappearance in the polar mesopause in the afternoon of 24 June 2024 has been analyzed. This cloud disappearance was caused by the localized warm spot in the mesopause region between Greenland and Scandinavia, as shown by Aura/MLS satellite and JAWARA model data. This warm spot in the mesopause region was caused by the intrusion of a warm air mass from middle to high latitudes.

7. Different movements of NLC were observed in the morning of 25 June 2024 over Greenland. One part of the clouds moved to NNE, another one moved to SSW. A detailed analysis of wind data based on the JAWARA model showed that there were different wind systems between 80 and 94 km altitude over Greenland, with a clockwise wind rotation with altitude. Most likely, a large inertia-gravity wave propagated upwards, causing significant disturbances (45–50 $\mathrm{m\,s^{-1}}$) of the horizontal wind. The wind disturbances caused NLC to move differently at different altitudes. Other mechanisms such as the vertical displacement of the NLC layer by gravity waves may explain the observed different NLC motions.

These results demonstrate the scientific value of long-duration stratospheric balloon missions for mesospheric research. Future campaigns of this type will benefit from expanded multi-spectral imaging, real-time data transmission, and coordinated ground–satellite observations to further improve understanding of mesospheric cloud dynamics. A statistical analysis of the wave dynamics observed in NLC during the 2024 TRANSAT balloon flight, and investigation of microphysical properties of NLC ice particles will be addressed in future studies.

Data availability. Two video files of the SONC experiment are available on the Harvard Dataverse repository (https://doi.org/10.7910/DVN/AKJK4P, Dalin, 2025b; https://doi.org/10.7910/DVN/1PHRZU, Dalin, 2025a). Individual NLC images taken from the stratosphere by the SONC experiment that support the findings of this study are available at the HEMERA Data Centre (https://data.hemera-h2020.eu/atmospheric-balloon-experiments/#/, last access: 27 April 2026) as well as will be made available on request.

Author contributions. PD, HS, NP, VP, JK and AR have designed two balloon-borne experiments dedicated to studies of noctilucent clouds and infrasound waves. PD wrote the draft of the paper and made analyses of the SONC images, Esrange lidar, Aura/MLS and JAWARA data. LM made analysis of the MATS satellite data. PV and JH performed Esrange lidar measurements. GB performed ALOMAR lidar measurements. DE designed and produced the electric control unit for the SONC imager. All authors discussed the results and contributed to revisions of the text and the figures.

Competing interests. The contact author has declared that none of the authors has any competing interests.

Acknowledgements. The authors thank the CNES/INSU-CNRS Balloon Programme. The TRANSAT balloon flight was funded and performed by the French Space Agency (CNES) (https://stratocat.com.ar/fichas-e/2024/KRN-20240622.htm, last access: 27 April 2026). The authors thank the Aura/MLS team for providing temperature and water vapor data around the globe during the 2024 TRANSAT balloon flight.

Financial support. The SONC imager hardware (imager and electronic control unit) was funded by the Kempe Foundation (Kempestiftelserna) under grant agreement JCK-1901.4. The infrasound instrument and flight costs of the SONC and infrasound instruments were financed under research grant 42/17 from the Swedish National Space Agency (Rymdstyrelsen). The MATS satellite and JH were financed by the Swedish National Space Agency under grant 2021-00052. LM was financed by the Swedish National Space Agency under grant 2022-00108 and the Swedish Research Council (Vetenskapsrådet) under grant 2021-04876.

The publication of this article was funded by the
Swedish Research Council, Forte, Formas, and Vinnova.

Review statement. This paper was edited by Petr Pisoft and reviewed by two anonymous referees.

References

Bailey, S. M., Thomas, G. E., Rusch, D. W., Merkel, A. W., Jeppesen, C., Carstens, J. N., Randall, C. E., McClintock, W. E., and Russell, J. M.: Phase functions of polar mesospheric cloud ice as observed by the CIPS instrument on the AIM satellite, J. Atmos. Sol.-Terr. Phy., 71, 373–380, https://doi.org/10.1016/j.jastp.2008.09.039, 2009.

Baumgarten, G.: Doppler Rayleigh/Mie/Raman lidar for wind and temperature measurements in the middle atmosphere up to 80 km, Atmos. Meas. Tech., 3, 1509–1518, https://doi.org/10.5194/amt-3-1509-2010, 2010.

Baumgarten, G. and Fritts, D. C.: Quantifying Kelvin-Helmholtz instability dynamics observed in noctilucent clouds: 1. Methods and observations, J. Geophys. Res.-Atmos., 119, 9324–9337, https://doi.org/10.1002/2014JD021832, 2014.

Baumgarten, G., Fiedler, J., Fricke, K. H., Gerding, M., Hervig, M., Hoffmann, P., Müller, N., Pautet, P.-D., Rapp, M., Robert, C., Rusch, D., von Savigny, C., and Singer, W.: The noctilucent cloud (NLC) display during the ECOMA/MASS sounding rocket flights on 3 August 2007: morphology on global to local scales, Ann. Geophys., 27, 953–965, https://doi.org/10.5194/angeo-27-953-2009, 2009.

Baumgarten, G., Chandran, A., Fiedler, J., Hoffmann, P., Kaifler, N., Lumpe, J., Merkel, A., Randall, C. E., Rusch, D., and Thomas, G.: On the horizontal and temporal structure of noctilucent clouds as observed by satellite and lidar at ALOMAR (69N), Geophys. Res. Lett., 39, L01803, https://doi.org/10.1029/2011GL049935, 2012.

Berger, U. and von Zahn, U.: Icy particles in the summer mesopause region: three-dimensional modeling of their environment and two-dimensional modeling of their transport, J. Geophys. Res., 107, 1366, https://doi.org/10.1029/2001JA000316, 2002.

Blum, U. and Fricke, K. H.: The Bonn University lidar at the Esrange: technical description and capabilities for atmospheric research, Ann. Geophys., 23, 1645–1658, https://doi.org/10.5194/angeo-23-1645-2005, 2005.

Chkhetiani, O. and Shalimov, S.: On anomalous wind amplitudes in the lower ionosphere, J. Atmos. Sol.-Terr. Phy., 240, 105960, https://doi.org/10.1016/j.jastp.2022.105960, 2022.

Chkhetiani, O. G. and Shalimov, S. L.: Helicity in the upper atmosphere and Ekman-type instabilities, Dokl. Earth Sc., 431, 345–350, https://doi.org/10.1134/S1028334X10030177, 2010.

Conte, J. F., Chau, J. L., Renkwitz, T., Latteck, R., Tsutsumi, M., Jacobi, C., Gulbrandsen, N., and Nozawa, S.: Observing mesoscale dynamics with multistatic specular meteor radars: first climatology of momentum flux, horizontal divergence and relative vorticity over northern central Europe, Ann. Geophys., 43, 603–619, https://doi.org/10.5194/angeo-43-603-2025, 2025.

Dalin, P.: Noctilucent clouds observed from the stratosphere during the 2024 TRANSAT balloon flight, Harvard Dataverse, V1 [data set], https://doi.org/10.7910/DVN/1PHRZU, 2025a.

Dalin, P.: Two layers in noctilucent clouds seen from the stratosphere during the 2024 TRANSAT balloon flight, Harvard Dataverse, V1 [data set], https://doi.org/10.7910/DVN/AKJK4P, 2025b.

Dalin, P., Pertsev, N., Zadorozhny, A., Connors, M., Schofield, I., Shelton, I., Zalcik, M., McEwan, T., McEachran, I., Frandsen, S., Hansen, O., Andersen, H., Sukhodoev, V., Perminov, V., and Romejko, V.: Ground-based observations of noctilucent clouds with a northern hemisphere network of automated digital cameras, J. Atmos. Sol.-Terr. Phy., 70, 1460–1472, https://doi.org/10.1016/j.jastp.2008.04.018, 2008.

Dalin, P., Pertsev, N., Frandsen, S., Hansen, O., Andersen, H., Dubietis, A., and Balciunas, R.: A case study of the evolution of a Kelvin-Helmholtz wave and turbulence in noctilucent clouds, J. Atmos. Sol.-Terr. Phy., 72, 1129–1138, https://doi.org/10.1016/j.jastp.2010.06.011, 2010.

Dalin, P., Pertsev, N., Dubietis, A., Zalcik, M., Zadorozhny, A., Connors, M., Schofield, I., McEwan, T., McEachran, I., Frandsen, S., Hansen, O., Andersen, H., Sukhodoev, V., Perminov, V., Balčiunas, R., and Romejko, V.: A comparison between ground-based observations of noctilucent clouds and Aura satellite data, J. Atmos. Sol.-Terr. Phy., 73, 2097–2109, https://doi.org/10.1016/j.jastp.2011.01.020, 2011.

Dalin, P., Pogoreltsev, A., Pertsev, N., Perminov, V., Shevchuk, N., Dubietis, A., Zalcik, M., Kulikov, S., Zadorozhny, A., Kudabayeva, D., Solodovnik, A., Salakhutdinov, G., and Grigoryeva, I.: Evidence of the formation of noctilucent clouds due to propagation of an isolated gravity wave caused by a tropospheric occluded front, Geophys. Res. Lett., 42, 2037–2046, https://doi.org/10.1002/2014GL062776, 2015.

Dalin, P., Pertsev, N., Perminov, V., Efremov, D., and Romejko, V.: Looking at "night-shining" clouds from the stratosphere, Eos–AGU, 100, https://doi.org/10.1029/2019EO118439, 2019.

Dalin, P., Pertsev, N., Perminov, V., Efremov, D., and Romejko, V.: Stratospheric observations of noctilucent clouds: a new approach in studying middle- and large-scale mesospheric dynamics, Ann. Geophys., 38, 61–71, https://doi.org/10.5194/angeo-38-61-2020, 2020.

Dalin, P., Suzuki, H., Pertsev, N., Perminov, V., Efremov, D., Voelger, P., Narayanan, V. L., Mann, I., Häggström, I., Zalcik, M., Ugolnikov, O., Hedin, J., Gumbel, J., Latteck, R., and Baumgarten, G.: Studies of noctilucent clouds from the stratosphere during the SONC balloon-borne experiment in 2021, J. Atmos. Sol.-Terr. Phy., 240, 105959, https://doi.org/10.1016/j.jastp.2022.105959, 2022.

DeLand, M. T. and Thomas, G. E.: Updated PMC trends derived from SBUV data, J. Geophys. Res.-Atmos., 120, 2140–2166, https://doi.org/10.1002/2014JD022253, 2015.

Demissie, T. D., Espy, P. J., Kleinknecht, N. H., Hatlen, M., Kaifler, N., and Baumgarten, G.: Characteristics and sources of gravity waves observed in noctilucent cloud over Norway, Atmos. Chem. Phys., 14, 12133–12142, https://doi.org/10.5194/acp-14-12133-2014, 2014.

Dubinskii, A. Yu. and Popel, S. I.: Formation and evolution of dusty plasma structures in the ionosphere, JETP Lett., 96, 21–26, https://doi.org/10.1134/S0021364012130048, 2012.

Eckermann, S. D.: Hodographic analysis of gravity waves: relationships among Stokes parameters, rotary spectra and cross-spectral methods, J. Geophys. Res., 101, 19169–19174, https://doi.org/10.1029/96JD01578, 1996.

Fiedler, J., Baumgarten, G., Berger, U., Hoffmann, P., Kaifler, N., and Lübken, F.-J.: NLC and the background atmosphere above ALOMAR, Atmos. Chem. Phys., 11, 5701–5717, https://doi.org/10.5194/acp-11-5701-2011, 2011.

Fritts, D. C., Wang, L., Baumgarten, G., Miller, A. D., Geller, M. A., Jones, G., Limon, M., Chapman, D., Didier, J., Kjellstrand, C. B., Araujo, D., Hillbrand, S., Korotkov, A., Tucker, G., and Vinokurov, J.: High-resolution observations and modeling of turbulence sources, structures, and intensities in the upper mesosphere, J. Atmos. Sol.-Terr. Phy., 162, 57–78, https://doi.org/10.1016/j.jastp.2016.11.006, 2017.

Fritts, D. C., Miller, A. D., Kjellstrand, C. B., Geach, C., Williams, B. P., Kaifler, B., Kaifler, N., Jones, G., Rapp, M., Limon, M., Reimuller, J., Wang, L., Hanany, S., Gisinger, S., Zhao, Y., Stober, G., and Randall, C. E.: PMC Turbo: Studying gravity wave and instability dynamics in the summer mesosphere using polar mesospheric cloud imaging and profiling from a stratospheric balloon, J. Geophys. Res.-Atmos., 124, 6423–6443, https://doi.org/10.1029/2019JD030298, 2019.

Froidevaux, L., Livesey, N. J., Read, W. G., Jiang, Y. B., Jiménez, C. C., Filipiak, M. J., Schwartz, M. J., Santee, M. L., Pumphrey, H. C., Jiang, J. H., Wu, D. L., Manney, G. L., Drouin, B. J., Waters, J. W., Fetzer, E. J., Bernath, P. F., Boone, C. D., Walker, K. A., Jucks, K. W., Toon, G. C., Margitan, J. J., Sen, B., Webster, C. R., Christensen, L. E., Elkins, J. W., Atlas, E., Lueb, R. A., and Hendershot, R.: Early validation analyses of atmospheric profiles from EOS MLS on the Aura satellite, IEEE T. Geosci. Remote, 44, 1106–1121, https://doi.org/10.1109/TGRS.2006.864366, 2006.

Gadsden, M. and Schröder, W.: Noctilucent Clouds, Springer, New York, https://doi.org/10.1007/978-3-642-48626-5, 1989.

Gao, H., Shepherd, G. G., Tang, Y., Bu, L., and Wang, Z.: Double-layer structure in polar mesospheric clouds observed from SOFIE/AIM, Ann. Geophys., 35, 295–309, https://doi.org/10.5194/angeo-35-295-2017, 2017.

Gerding, M., Höffner, J., Hoffmann, P., Kopp, M., and Lübken, F.-J.: Noctilucent cloud variability and mean parameters from 15 years of lidar observations at a mid-latitude site (54°N, 12°E), J. Geophys. Res.-Atmos., 118, 317–328, https://doi.org/10.1029/2012JD018319, 2013.

Gossard, E. E. and Hooke, W. H.: Waves in the atmosphere: atmospheric infrasound and gravity waves – their generation and propagation, Elsevier Scientific Publishing Co, Amsterdam, https://www.amazon.com/Waves-Atmosphere-Atmospheric-Propagation-Developments/dp/0444411968 (last access: 27 April 2026), 1975.

Gumbel, J. and Witt, G.: Rocket-borne photometry of NLC particle populations, Adv. Space Res., 28, 1053–1058, https://doi.org/10.1016/S0273-1177(01)80036-3, 2001.

Gumbel, J., Megner, L., Christensen, O. M., Ivchenko, N., Murtagh, D. P., Chang, S., Dillner, J., Ekebrand, T., Giono, G., Hammar, A., Hedin, J., Karlsson, B., Krus, M., Li, A., McCallion, S., Olentšenko, G., Pak, S., Park, W., Rouse, J., Stegman, J., and Witt, G.: The MATS satellite mission – gravity wave studies by Mesospheric Airglow/Aerosol Tomography and Spectroscopy, Atmos. Chem. Phys., 20, 431–455, https://doi.org/10.5194/acp-20-431-2020, 2020.

Hervig, M. E., Siskind, D. E., Bailey, S. M., and Russell III, J. M.: The influence of PMCs on water vapor and drivers behind PMC variability from SOFIE observations, J. Atmos. Sol.-Terr. Phy., 132, 124–134, https://doi.org/10.1016/j.jastp.2015.07.010, 2015.

Kaifler, N., Baumgarten, G., Klekociuk, A. R., Alexander, S. P., Fiedler, J., and Lübken, F.-J.: Small scale structures of NLC observed by lidar at 69°N/69°S and their possible relation to gravity waves, J. Atmos. Sol.-Terr. Phy., 104, 244–252, https://doi.org/10.1016/j.jastp.2013.01.004, 2013.

Karlsson, B. and Gumbel, J.: Challenges in the limb retrieval of noctilucent cloud properties from Odin/OSIRIS, Adv. Space Res., 36, 935–942, https://doi.org/10.1016/j.asr.2005.04.074, 2005.

Koshin, D., Sato, K., Miyazaki, K., and Watanabe, S.: An ensemble Kalman filter data assimilation system for the whole neutral atmosphere, Geosci. Model Dev., 13, 3145–3177, https://doi.org/10.5194/gmd-13-3145-2020, 2020.

Koshin, D., Sato, K., Kohma, M., and Watanabe, S.: An update on the 4D-LETKF data assimilation system for the whole neutral atmosphere, Geosci. Model Dev., 15, 2293–2307, https://doi.org/10.5194/gmd-15-2293-2022, 2022.

Koshin, D., Sato, K., Watanabe, S., and Miyazaki, K.: The JAGUAR-DAS whole neutral atmosphere reanalysis: JAWARA, Prog. Earth Planet. Sci., 12, 1, https://doi.org/10.1186/s40645-024-00674-3, 2025.

Lambert, A., Read, W. G., Livesey, N. J., Santee, M. L., Manney, G. L., Froidevaux, L., Wu, D. L., Schwartz, M. J., Pumphrey, H. C., Jimenez, C., Nedoluha, G. E., Cofield, R. E., Cuddy, D. T., Daffer, W. H., Drouin, B. J., Fuller, R. A., Jarnot, R. F., Knosp, B. W., Pickett, H. M., Perun, V. S., Snyder, W. V., Stek, P. C., Thurstans, R. P., Wagner, P. A., Waters, J. W., Jucks, K. W., Toon, G. C., Stachnik, R. A., Bernath, P. F., Boone, C. D., Walker, K. A., Urban, J., Murtagh, D., Elkins, J. W., and Atlas, E.: Validation of the Aura Microwave Limb Sounder middle atmosphere water vapor and nitrous oxide measurements, J. Geophys. Res., 112, D24S36, https://doi.org/10.1029/2007JD008724, 2007.

Li, H., Wu, J., and Zhou, Z.: The formation of multiple layers of ice particles in the polar summer mesopause region, Ann. Geophys., 34, 117–122, https://doi.org/10.5194/angeo-34-117-2016, 2016.

Liu, X., Yue, J., Xu, J., Yuan, W., Russell III, J. M., Hervig, M. E., and Nakamura, T.: Persistent longitudinal variations in 8 years of CIPS/AIM polar mesospheric clouds, J. Geophys. Res.-Atmos., 121, 8390–8409, https://doi.org/10.1002/2015JD024624, 2016.

Megner, L., Gumbel, J., Christensen, O. M., Linder, B., Murtagh, D., Ivchenko, N., Krasauskas, L., Hedin, J., Dillner, J., and Stegman, J.: MATS satellite images (level 1b) of airglow and noctilucent clouds in the mesosphere/lower thermosphere, February–May 2023, Dataset version 1.0, Bolin Centre Database [data set], https://doi.org/10.17043/mats-level-1b-limb-cropd-1.0, 2025.

Miller, A. D., Fritts, D. C., Chapman, D., Jones, G., Limon, M., Araujo, D., Didier, J., Hillbrand, S., Kjellstrand, C. B., Korotkov, A., Tucker, G., Vinokurov, Y., Wan, K., and Wang, L.: Stratospheric imaging of polar mesospheric clouds: a new window on small-scale atmospheric dynamics, Geophys. Res. Lett., 42, 6058–6065, https://doi.org/10.1002/2015GL064758, 2015.

Murphy, D. M. and Koop, T.: Review of the vapour pressures of ice and supercooled water for atmospheric applications, Q. J. Roy. Meteor. Soc., 131, 1539–1565, https://doi.org/10.1256/qj.04.94, 2005.

Pautet, P.-D., Stegman, J., Wrasse, C. M., Nielsen, K., Takahashi, H., Taylor, M. J., Hoppel, K. W., and Eckermann, S. D.: Analysis of gravity waves structures visible in noctilucent cloud images, J. Atmos. Sol.-Terr. Phy., 73, 2082–2090, https://doi.org/10.1016/j.jastp.2010.06.001, 2011.

Pertsev, N. N., Dalin, P. A., Perminov, V. I., Gusev, N. K., Tsimerinov, E. Yu., Solodovnik, A. A., Zadorozhny, A. M., Korotyshkin, D. V., and Bordonskiy, G. S.: Analysis of noctilucent cloud fields according to ground-based network and airborne photography data, Izv. Atmos. Ocean. Phys., 60, 187–194, https://doi.org/10.1134/S0001433824700191, 2024.

Portnyagin, Y. I. and Solovjova, T. V.: Global empirical wind model for the upper mesosphere/lower thermosphere. I. Prevailing wind, Ann. Geophys., 18, 300–315, https://doi.org/10.1007/s00585-000-0300-y, 2000.

Randall, C. E., Carstens, J., France, J. A., Harvey, V. L., Hoffmann, L., Bailey, S. M., Alexander, M. J., Lumpe, J. D., Yue, J., Thurairajah, B., Siskind, D. E., Zhao, Y., Taylor, M. J., and Russell III, J. M.: New AIM/CIPS global observations of gravity waves near 50–55 km, Geophys. Res. Lett., 44, 7044–7052, https://doi.org/10.1002/2017GL073943, 2017.

Rapp, M., Lubken, F.-J., Müllemann, A., Thomas, G. E., and Jensen, E. J.: Small-scale temperature variations in the vicinity of NLC: Experimental and model results, J. Geophys. Res., 107, 4392, https://doi.org/10.1029/2001JD001241, 2002.

Read, W. G., Lambert, A., Bacmeister, J., Cofield, R. E., Christensen, L. E., Cuddy, D. T., Daffer, W. H., Drouin, B. J., Fetzer, E., Froidevaux, L., Fuller, R., Herman, R., Jarnot, R. F., Jiang, J. H., Jiang, Y. B., Kelly, K., Knosp, B. W., Kovalenko, L. J., Livesey, N. J., Liu, H.-C., Manney, G. L., Pickett, H. M., Pumphrey, H. C., Rosenlof, K. H., Sabounchi, X., Santee, M. L., Schwartz, M. J., Snyder, W. V., Stek, P. C., Su, H., Takacs, L. L., Thurstans, R. P., Vömel, H., Wagner, P. A., Waters, J. W., Webster, C. R., Weinstock, E. M., and Wu, D. L.: Aura Microwave Limb Sounder upper tropospheric and lower stratospheric H_2O and relative humidity with respect to ice validation, J. Geophys. Res., 112, D24S35, https://doi.org/10.1029/2007JD008752, 2007.

Reimuller, J. D., Thayer, J. P., Baumgarten, G., Chandran, A., Hulley, B., Rusch, D., Nielsen, K., and Lumpe, J.: Synchronized imagery of noctilucent clouds at the day-night terminator using airborne and spaceborne platforms, J. Atmos. Sol.-Terr. Phy., 73, 2091–2096, https://doi.org/10.1016/j.jastp.2010.11.022, 2011.

Schwartz, M. J., Lambert, A., Manney, G. L., Read, W. G., Livesey, N. J., Froidevaux, L., Ao, C. O., Bernath, P. F., Boone, C. D., Cofield, R. E., Daffer, W. H., Drouin, B. J., Fetzer, E. J., Fuller, R. A., Jarnot, R. F., Jiang, J. H., Jiang, Y. B., Knosp, B. W., Krüger, K., Li, J.-L. F., Mlynczak, M. G., Pawson, S., Russell III, J. M., Santee, M. L., Snyder, W. V., Stek, P. C., Thurstans, R. P., Tompkins, A. M., Wagner, P. A., Walker, K. A., Waters, J. W., and Wu, D. L.: Validation of the Aura Microwave Limb Sounder temperature and geopotential height measurements, J. Geophys. Res., 113, D15S11, https://doi.org/10.1029/2007JD008783, 2008.

Suzuki, H., Matsumoto, A., Dalin, P., Nakamura, Y., Ishii, S., Sakanoi, K., Sakaguchi, K., Takada, T., Tsuda, T. T., and Hozumi, Y.: Capability of airline jets as an observation platform for noctilucent clouds at middle latitudes, Prog. Earth Planet. Sci., 9, 11, https://doi.org/10.1186/s40645-022-00469-4, 2022.

Thomas, G. E.: Solar Mesosphere Explorer measurements of polar mesospheric clouds (noctilucent clouds), J. Atmos. Terr. Phys., 46, 819–824, 1984.

Tsuda, T. T., Hozumi, Y., Kawaura, K., Tatsuzawa, K., Ando, Y., Hosokawa, K., Suzuki, H., Murata, K. T., Nakamura, T., Yue, J., and Nielsen, K.: Detection of polar mesospheric clouds utilizing Himawari-8/AHI full-disk images, Earth Space Sci., 9, 2021EA002076, https://doi.org/10.1029/2021EA002076, 2022.

Wallis, S., DeLand, M., and von Savigny, C.: Did the 2022 Hunga eruption impact the noctilucent cloud season in 2023/24 and 2024?, Atmos. Chem. Phys., 25, 3635–3645, https://doi.org/10.5194/acp-25-3635-2025, 2025.

Zadorozhny, A. M., Tyutin, A. A., Witt, G., Wilhelm, N., Wälchli, U., Cho, J. Y. N., and Swartz, W. E.: Electric field measurements in the vicinity of noctilucent clouds and PMSE, Geophys. Res. Lett., 20, 2299–2302, https://doi.org/10.1029/93GL02626, 1993.